Chemical Science

ROYAL SOCIETY OF CHEMISTRY

REVIEW

View Article Online
View Journal | View Issue

Cite this: *Chem. Sci.*, 2025, **16**, 16483

Plasmonic photothermal nanomaterials for solar steam generation

Yong Wang, [ab] Guozhu Chen, [c] Mohamed Chaker[a] and Dongling Ma *[a]

Solar steam generation, a sustainable and cost-effective water purification technique, has emerged as a promising solution to the global freshwater shortage. Plasmonic photothermal nanomaterials (NMs) have recently garnered enormous attention owing to their strong light–matter interactions and high photothermal conversion efficiency. This review begins by outlining the fundamentals of the plasmonic effect. Subsequently, we classify the current solar steam generation systems and discuss the critical parameters governing their performance. Recent advancements in plasmon-empowered NMs are then summarized according to five major classes: metals, metal nitrides, metal chalcogenides, metal oxides, and MXenes. Furthermore, this review highlights four primary applications of plasmon-driven solar steam generation. Finally, it discusses existing challenges in this research field and provides perspectives on future research directions. This comprehensive review offers valuable insights into the rational design and fabrication of plasmonic NMs for efficient solar steam generation and can thus serve as a guide for future development in this field.

Received 7th May 2025
Accepted 16th August 2025

DOI: 10.1039/d5sc03309h

rsc.li/chemical-science

1. Introduction

Freshwater has been a basic necessity of human life since ancient times. In reality, however, people in many regions still face severe freshwater shortages, sometimes so extreme that they threaten basic human survival.[1] Although 70% of the Earth's surface is covered by water, only a small portion (3%) is freshwater.[2] Population growth, urbanization, climate change, environmental pollution, and energy crises further exacerbate the challenge of clean water scarcity. To address this issue, various technologies, including electrodialysis,[3] reverse osmosis,[4] thermal distillation,[5] and membrane distillation,[6] have been developed to purify non-potable water sources into clean, drinking water. Nonetheless, these traditional purification methods often require high energy consumption (*e.g.*, electricity, thermal energy, mechanical energy, *etc.*), expensive materials, and/or complex infrastructure, leading to not only high operational costs but also negative secondary environmental impacts. Thus, it is urgent to develop green, cost-effective and energy-efficient water purification technologies to meet the global demand for freshwater. As a non-exhaustible green energy, solar energy has attracted extensive interest and been widely used across diverse applications. Recently, solar steam generation has emerged as a promising and sustainable solution to tackle water scarcity, and in particular its application in freshwater production through wastewater treatment and seawater desalination has been extensively studied.[7–11] This environment-friendly photothermal technology harnesses solar energy to heat water molecules, transitioning them from liquid to vapor (steam). To date, considerable efforts have been devoted to developing solar steam generation materials, devices and processes in order to improve the efficiency of clean freshwater production.

The key to the effectiveness of any solar steam generation system lies in the photothermal material, which absorbs solar energy and converts it into heat, driving water evaporation. To date, numerous photothermal nanomaterials (NMs) have been explored, including carbon-based NMs, plasmonic NMs, semiconductors, and organic polymers.[12–17] Among these materials, plasmonic photothermal NMs have aroused widespread interest owing to their strong light–matter interactions, which enable enhanced solar harvesting and efficient photothermal conversion. Several advantages make plasmonic NMs more promising for efficient solar steam generation: (i) enhanced solar absorption arising from multiple optical transition processes; (ii) tunable absorption spectra, allowing for optimal spectral matching with solar radiation; (iii) locally strong light–matter interactions and electromagnetic fields, minimizing energy loss; and (iv) robust and efficient photothermal conversion capabilities, conducive to improving solar utilization. Despite these advantages, the full potential of plasmon-driven solar steam generation remains largely untapped. Therefore, a thorough analysis of existing plasmonic photothermal materials used in solar water evaporation is essential to guide future research and development in this field.

[a]*Institut National de la Recherche Scientifique, 1650 Boulevard Lionel Boulet, Varennes J3X 1P7, Canada. E-mail: dongling.ma@inrs.ca*

[b]*Ganjiang Innovation Academy, Chinese Academy of Sciences, Ganzhou 341119, China*

[c]*School of Chemistry and Chemical Engineering, University of Jinan, Jinan 250022, China*

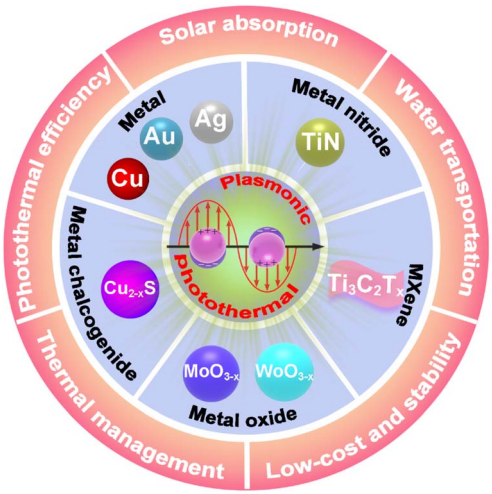

Fig. 1 Summary of plasmonic photothermal NMs and key design principles for solar steam generation.

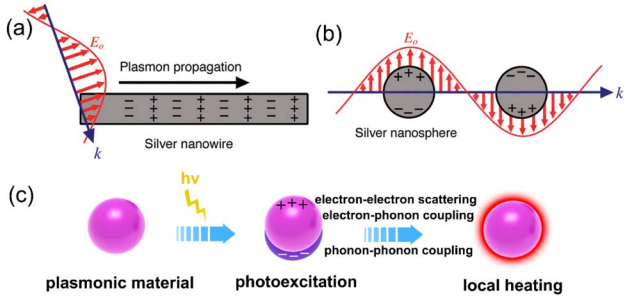

Fig. 2 Schematic illustration of the two types of plasmonic nanostructures, as excited by the electric field (E_o) of incident light with wavevector (k). In (a), the nanowire has one dimension much larger than the wavelength of light. In this case, light coupled to the nanostructure will excite the free electrons to create a propagating surface plasmon that can travel along the surface of the metal nanostructure. In (b), the nanostructure is smaller than the wavelength of light, and the free electrons can be displaced from the lattice of positive ions (consisting of nuclei and core electrons) and collectively oscillate in resonance with the light. This is known a localized surface plasmon resonance (LSPR). Reproduced with permission.[24] Copyright 2011, American Chemical Society. (c) Schematic describing the photothermal conversion process.

Recently, significant advancements have been made in the areas of plasmonic photothermal NMs and system designs for solar steam generation, including advanced plasmonic materials for enhanced photothermal conversion, novel plasmonic system configurations for improved energy harvesting, and new strategies in plasmonic material optimization. This review aims to provide an updated and in-depth analysis of these recent developments in plasmonic photothermal NMs for solar steam generation, offering a fresh perspective on the current state-of-the-art. As illustrated in Fig. 1, the reported plasmonic photothermal NMs for solar steam generation are mainly classified into five categories: (1) plasmonic metals; (2) plasmonic metal nitrides; (3) plasmonic metal chalcogenides; (4) plasmonic metal oxides; and (5) plasmonic MXenes. Additionally, Fig. 1 highlights five key design principles for plasmonic solar absorbers that should be holistically optimized to improve their solar steam generation performance: (1) solar absorption; (2) photothermal efficiency; (3) water transportation; (4) low-cost and stability; and (5) thermal management.

2. Fundamentals of plasmonics and the photothermal process

2.1. Principles of plasmonic effects

The well-known plasmonic effects originate from the collective oscillation of free charge carriers induced by light–matter interactions.[18] Plasmons are generally categorized into two types: surface plasmon polaritons (SPP) and localized surface plasmon resonance (LSPR). SPP can propagate dozens or hundreds of micrometers along a metal–dielectric interface, with a decay depth of ~200 nm (Fig. 2a).[19] In contrast, LSPR is confined to the nanoparticle (NP) surface (Fig. 2b). The excited surface plasmons decay *via* different pathways, including electron–phonon coupling, electron–electron scattering, and phonon–phonon coupling, most of which are eventually dissipated as heat (Fig. 2c).[20] In the initial stage (<100 fs), immediately following the photoexcitation of plasmonic metal NPs, electron–electron scattering results in the redistribution of hot electrons.[21] This is followed by the ultrafast heating through electron–lattice phonon coupling. Finally, the generated heat is dissipated into the surrounding medium by phonon–phonon coupling on a timescale of several hundreds of picoseconds.[22,23]

2.2. Intrinsic properties of plasmonic NMs

The LSPR properties of plasmonic NMs are closely linked to their free charge carriers (electrons or holes). Plasmonic metal NMs (*e.g.*, Al, Pt, Au, Ag, and Cu) have extremely high free electron densities (on the order of 10^{22} cm^{-3} or above) due to their metallic nature, leading to the inherent LSPR frequencies within the ultraviolet (UV) and visible regions of the electromagnetic spectrum.[25,26] In plasmonic metal NPs, the free charge carrier density almost remains constant and is insensitive to any external environments. Similarly, metal nitrides (TiN, ZrN, and HfN) have high free electron densities (on the order of 10^{22} cm^{-3}), and their dielectric permittivities have a zero crossing wavelength in the visible region, enabling broad LSPR spanning the visible and near-infrared (NIR) regions.[27,28] MXenes, such as $Ti_3C_2T_x$, also exhibit attractive LSPR effects due to their relatively high carrier densities (on the order of 10^{21} cm^{-3}), arising from their unique chemical bonding, electronic structure, layered structure, and strong absorption of electromagnetic waves.[29] Their efficient light absorption across a broad spectral range (visible to NIR) is attributed to strong electron–phonon collisions with a large absorption cross-section and an ultrathin atomic layer structure. Different from these three types, plasmonic metal chalcogenide NMs (*e.g.*, $Cu_{2-x}E$, where E = S, Se, and Te) possess free holes, generated by the introduction of cation vacancies. Covellite CuS NPs present an exception, exhibiting LSPR attributed to free holes associated with disulfide bonds.[30] With a slightly lower hole density, their LSPR peaks are usually located

in the NIR range. As for plasmonic metal oxide NMs (*e.g.*, WO_{3-x} and MoO_{3-x}), their free electrons are generated by oxygen vacancies. The free charge carrier density of metal chalcogenides and metal oxides is widely tunable ($\sim 10^{19}$–10^{22} cm^{-3}) by changing the cation or oxygen vacancies, thereby allowing adjustable LSPR from the NIR to mid-IR regions.[25,26,31]

2.3. Factors influencing plasmonic effects

Beyond the intrinsic material properties, the plasmonic behavior of NMs is largely influenced by their size, shape, composition, and surrounding dielectric environments (Fig. 3).[32,33] These factors collectively dictate the light absorption of plasmonic NMs, and further affect their photothermal conversion efficiency. For example, different plasmonic NMs exhibit distinct LSPR peak positions (Fig. 3a). Ag nanospheres typically display an LSPR peak at ~412 nm, while Au and Cu nanospheres of similar sizes exhibit LSPR peaks at ~520 nm and ~576 nm, respectively.[34–36] Fig. 3b shows the size-dependent effect on the LSPR band, where the LSPR peak generally shifts to longer wavelengths as the NP size increases. As demonstrated by Halas *et al.*, a large shift of 18 nm occurred when the size of Au NPs increased from 30 to 100 nm.[37] As the size of Au NPs increased further, phase retardation led to a reduction in wavelength shift. Additionally, anisotropic NPs often exhibit multiple LSPR peaks.[38] For example, Au nanorods typically exhibit two distinct LSPR peaks: a shorter-wavelength peak at ~520 nm, corresponding to the transverse mode, and a longer-wavelength peak at ~760 nm, indexed to the longitudinal plasmon mode (Fig. 3c). Furthermore, the LSPR peak can be effectively tuned by modifying the composition of plasmonic NPs. For instance, Au–Ag alloys with varying Au : Ag ratios exhibited LSPR peaks that lie between those of pure Au and Ag NPs (Fig. 3d).[39] In anisotropic plasmonic nanostructures, changing the aspect ratio also affects the LSPR peak. For example, the longitudinal resonance peak of Au nanorods shifted from the visible to NIR region as the aspect ratio increased from 2.4 to 5.6 (Fig. 3e).[40]

The LSPR also varies with NP coupling. Fig. 3f shows that the simulated absorption spectra of Au nanosphere dimers (nanosphere diameter: 50 nm) exhibit a redshift from ~530 to ~620 nm as the interparticle distance decreases from 100 to 2 nm.[41] Additionally, the LSPR intensity is significantly enhanced under parallel polarization, and a distinct resonance feature appears when the distance is reduced to 2 nm. Plasmonic coupling *via* near-field interactions results in spectral splitting and broadening, which can enhance the solar thermal conversion efficiency.[21] Moreover, it is well known that the LSPR peak positions of plasmonic NMs shift with the local refractive index of the surrounding dielectric media, enabling their application as sensors. Recently, Shen *et al.* fabricated a periodic array of Au mushrooms, consisting of the Au cap, photoresist pillar, and Au film, as a plasmonic biosensor for detecting alpha-fetoprotein and cytochrome c by measuring the local refractive index changes through LSPR.[42]

Moreover, for plasmonic metal nitrides, the degree of oxidation (*e.g.*, TiN_xO_y) has great influence on their LSPR characteristics, as their LSPR originates from free electrons within the partially filled d-band of metal-like nitrides. TiN NMs, in

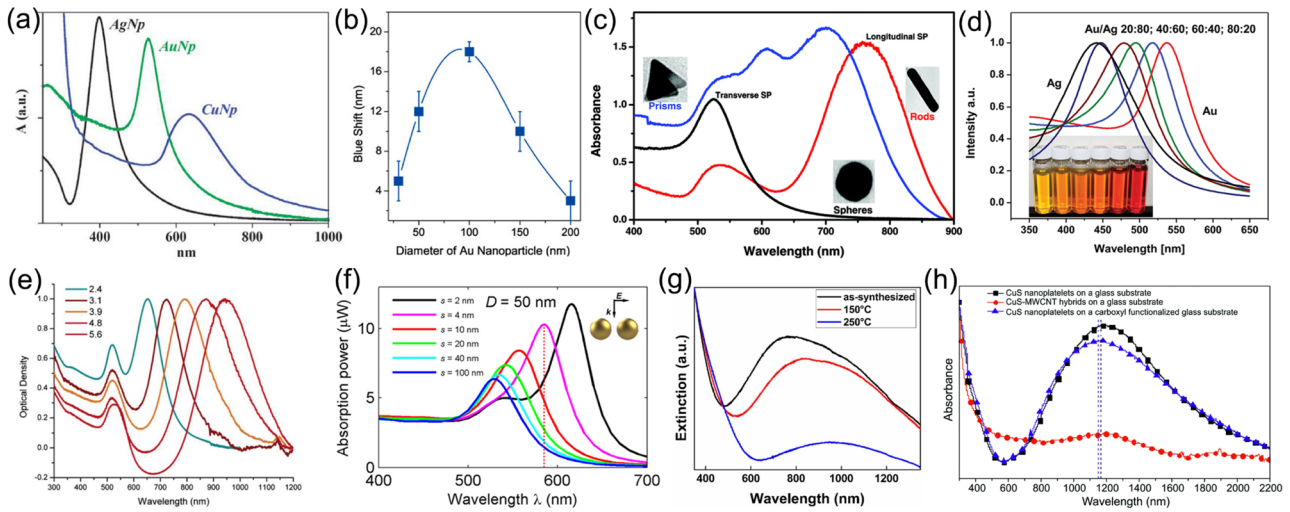

Fig. 3 The effect of various important factors on optical properties of plasmonic NMs. (a) Typical ultraviolet-visible-near infrared (UV-Vis-NIR) spectra of Ag, Au and Cu NPs obtained by LASiS (laser ablation synthesis in solution). Reproduced with permission.[45] Copyright 2009, Royal Society of Chemistry. (b) Dependence of nanobubble-induced LSPR blue shift on Au NP diameter. Reproduced with permission.[37] Copyright 2013, American Chemical Society. (c) Typical absorption spectra of Au NPs with different shapes. Reproduced with permission.[38] Copyright 2015, Royal Society of Chemistry. (d) Experimental spectra for different compositions of 60 nm Au/Ag alloy NPs. Reproduced with permission.[39] Copyright 2014, Royal Society of Chemistry. (e) Surface plasmon absorption spectra of Au nanorods of different aspect ratios. Reproduced with permission.[40] Copyright 2006, American Chemical Society. (f) Absorption spectra of Au nanosphere dimers of varying interparticle spacing for incident light polarized parallel to the interparticle axis. Reproduced with permission.[41] Copyright 2013, Optical Society of America. (g) Extinction measurements on ~8 nm TiN NPs before and after air annealing at 150 and 250 °C. Reproduced with permission.[43] Copyright 2017, American Chemical Society. (h) UV-Vis-NIR absorption spectra of CuS nanoplatelets and CuS–MWCNT hybrids deposited on glass substrates and CuS nanoplatelets deposited on a carboxyl functionalized glass substrate. Reproduced with permission.[44] Copyright 2016, Royal Society of Chemistry.

particular, typically display a broad LSPR band in visible and NIR regions, with both the peak position and intensity undergoing a redshift and weakening, respectively, as the oxidation degree increases (Fig. 3g).[43] Semiconductors, such as metal oxides and metal chalcogenides, demonstrate defect-dependent LSPR properties.[25] Their free charge carrier density can be easily tuned *via* varying the stoichiometry. Notably, the LSPR of plasmonic semiconductors is more sensitive to environments and can be quenched. For instance, our group observed that the LSPR of plasmonic CuS underwent significant changes when hybridized with multi-walled carbon nanotubes (MWCNTs) (Fig. 3h).[44] This phenomenon was attributed to the charge transfer between CuS and MWCNTs, which nearly completely quenched the LSPR. In brief, by strategically tuning the size, morphology, structure, defect concentration, and composition, it is possible to enhance and broaden the solar absorption capabilities of plasmonic NPs, thereby improving solar-thermal performance.

2.4. Photothermal effect of plasmonic NMs

The photothermal effect induced by LSPR was recognized when El-Sayed *et al.* demonstrated the reshaping of Au nanorods into nanospheres by heat generated under femtosecond laser irradiation.[46] Due to the strong correlation between the photothermal and optical properties of plasmonic NMs, their photothermal effect can be effectively enhanced by tuning the plasmonic resonance. For example, Lalisse *et al.* calculated the photothermal conversion efficiency of plasmonic NMs based on dielectric functions using Faraday and Joule numbers,[47] revealing that ZrN exhibits superior photothermal efficiency in the visible region, even comparable to Au or Cu. Furthermore, theoretical calculations have demonstrated size-dependent photothermal properties, revealing that the temperature increase of Au NPs is proportional to their size.[48] The shape-dependent photothermal properties of different Au nanostructures were also demonstrated using Green's dyadic method,[49] revealing that nanorods exhibit significantly higher heating efficiency than nanospheres, with the efficiency increasing proportionally to the nanorod aspect ratio. In addition, the corners and sharp edges of Au nanostructures have been shown to favor heat generation. These experimental and theoretical findings have contributed significantly to the design and synthesis of plasmonic NMs with high photothermal efficiency. More importantly, the photothermal efficiency, a critical factor for plasmonic NMs in photothermal applications, can be quantified by directly monitoring the temperature variation of their aqueous dispersions under alternating laser illumination and dark conditions.[50] This method has been widely used to calculate the photothermal conversion efficiency of various NMs under single-wavelength light illumination (Table 1).

Table 1 Photothermal conversion efficiency of various NMs reported in the literature

Material	Irradiation wavelength (nm)	Incident power (W cm^{-2})	Efficiency (%)	Ref.
Au nanorods	808	2	50.0	51
Au nanoshells	808	2	25.0	51
TiN NPs	808	2.27	38.1	52
$Cu_{2-x}Se$ NPs	800	2	22.0	53
Cu_9S_5 NPs	980	0.51	25.7	54
Carbon dots	635	2	36.2	55
MoO_{3-x} quantum dots	880	2	25.5	56
CuS/SiO_2 nanocapsules	980	1	31.2	57
Pt spirals	1120	—	52.5	58

3. Assessment and dominant factors of solar steam generation

3.1. Evaluation of solar steam generation

In a typical solar steam generation process, photothermal NMs absorb solar energy and convert it into thermal energy, which subsequently heats the surrounding water molecules, inducing vaporization. Thus, the performance of solar steam generation is primarily evaluated using two key parameters: the water evaporation rate and photothermal conversion efficiency. The evaporation rate quantifies the amount of vapour evaporated per unit area per unit time (kg m^{-2} h^{-1}) and can be calculated using the following equation

$$\dot{m} = \frac{M}{TA} \quad (1)$$

where $\dot{m}$ represents the evaporation rate, T denotes the evaporation time (h), M is the mass of evaporated water (kg), and A denotes the absorber area under illumination (m^{-2}).

The corresponding photothermal conversion efficiency (η) can be further calculated as follows:[59]

$$\eta = \frac{\dot{m}h_{\text{total}}}{C_{\text{opt}}q_{\text{i}}} \quad (2)$$

where h_{total} represents the total energy required for the phase change, C_{opt} represents the solar concentration, which is the ratio of solar radiation incident on the absorber surface to the nominal solar density (typically set to 1), and q_{i} denotes the nominal solar density of 1 kW m^{-2} (1 sun).

3.2. Systems of solar steam generation

Based on the integration design of plasmonic NMs, solar steam generation systems can be classified into two types (Fig. 4): (1) the suspending system, where plasmonic NMs are dispersed within an aqueous solution, and (2) the floating system, also referred to as the interfacial system, where plasmonic photothermal NMs are floating on a liquid surface. The suspending system, while traditional, is less efficient. For instance, Halas *et al.* introduced plasmonic SiO_2@Au core@shell NPs with broadband absorption in a suspending system.[60] It showed a water evaporation rate of <0.036 kg h^{-1} and water temperature increase of ~48 °C, attributed to the excellent thermal conductivity and LSPR effect of Au NPs. However, due to the significant heat loss inherent to the suspending system, it exhibited a low photothermal conversion efficiency of 24%

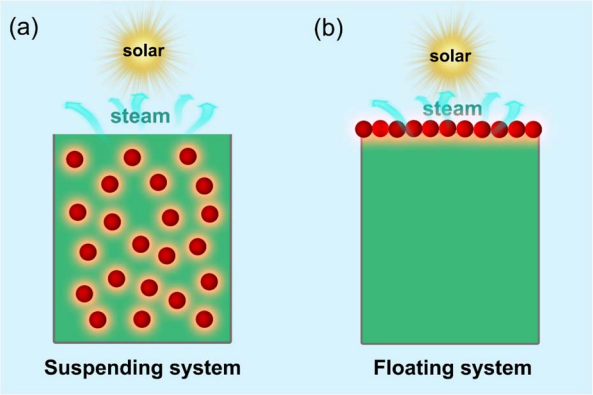

Fig. 4 Illustration of (a) suspending system and (b) floating system for solar steam generation.

under irradiation of 1.4 suns. In contrast, the floating system offers distinct advantages, primarily by localizing the generated heat at the water–air interface, thereby minimizing heat dissipation to the bulk water below. Bae *et al.* fabricated thin Au membranes through a self-assembly method involving anodization, wet etching, and sputtering.[61] Under 1 sun irradiation, the use of the floating Au membrane led to a much higher evaporation rate of 0.67 kg m^{-2} h^{-1} and a significantly enhanced photothermal efficiency of 42%, thanks to the minimized heat loss.

3.3. Factors influencing solar steam generation performance

The design of efficient solar absorbers for solar steam generation requires careful consideration of several critical factors, including solar absorption, photothermal efficiency, water transport, thermal management, stability, and cost (Fig. 1). Specifically, the solar absorption of plasmonic photothermal NMs plays a pivotal role in energy conversion. The light absorption range can be broadened by rationally adjusting the structure and composition of plasmonic NMs. Their combination with other photothermal NMs can further enhance the full-spectrum light absorption. The rational design and optimization of the solar absorber structure can also effectively minimize the light transmission and reflection. Therefore, photothermal efficiency can be improved by adjusting parameters such as size, morphology, composition, and defect concentration,[62] as partially demonstrated in Table 1.

Moreover, a continuous and sufficient water supply is also crucial for maximizing the evaporation capacity of solar absorbers.[59] In floating systems, water is continuously transported to the evaporation interface by the capillary wicking effect of porous structures. Recent studies have demonstrated that micro-sized pores are particularly effective for efficient capillary water transport.[63] Additionally, the hydrophilic properties of solar absorbers facilitate the uniform delivery of water molecules across the entire evaporation interface. However, excessively small pores and superhydrophilic surfaces can strongly bind adsorbed water, potentially reducing the evaporation rate.[62] Therefore, optimizing the pore size and hydrophilicity is essential to achieve rapid water replenishment and enhance the evaporation rate.

Effective thermal management is also critical, as it addresses heat loss, which primarily arises from downward thermal conduction to bulk water, upward thermal convection to the environment, and upward irradiative energy loss. During solar steam generation, the dissipation of generated heat to bulk water through NM or water conduction is the primary cause of heat loss. To mitigate it, insulated solar absorbers should be developed to inhibit the heat loss to bulk water. As for upward thermal convection and radiation losses, they are inherently present, and minimizing them without compromising other factors remains challenging. However, it has been reported that low-temperature evaporation or the use of spectrum-selective plasmonic absorbers can effectively reduce radiative losses.[7,13] In addition, three-dimensional (3D) solar absorbers with low thermal conductivity can effectively localize the generated heat at the evaporation interface, further reducing heat loss.[64]

Finally, the economic viability and stability of plasmonic NMs warrant significant attention for their practical applications. The long-term functionality of solar steam generation systems depends not only on the mechanical and chemical robustness of the NMs but also on their thermal stability under continuous irradiation. Performance degradation can result from various factors, including the dissolution, detachment, agglomeration, oxidation, and corrosion of plasmonic NPs, as well as the breakage of plasmonic films or NP assemblies. Recent advancements, such as the design of plasmonic core@shell structures, and the integration of plasmonic NMs with organic materials or other cost-effective photothermal NMs, have significantly improved the stability, sustainability, practicability, and photothermal performance. Nevertheless, the development of durable plasmonic composite photothermal NMs with exceptional photothermal performance for long-term, efficient solar steam generation still requires rational design strategies and substantial systematic optimization.

4. Plasmonic NMs for solar steam generation

To date, a variety of plasmonic NMs have been explored for solar steam generation, including metals,[61,65–82] metal nitrides,[83–89] metal chalcogenides,[90–94] metal oxides,[95–97] and MXenes.[98] This section will focus on these five types of plasmonic photothermal NMs, briefly discussing their solar absorption capacity, photothermal conversion efficiency, stability, and economic viability.

4.1. Plasmonic metals

Metallic plasmonic NMs (*e.g.*, Au, Ag, Cu, Pd, and Al) have been intensively explored as photothermal NMs for solar steam generation, owing to their strong LSPR effect. Among these, Au NPs are the most widely investigated due to their strong LSPR intensity, structural controllability, chemical stability, and facile synthesis. Since Halas *et al.* pioneered the application of plasmonic Au NPs in solar steam generation,[60,99] numerous

Table 2 Solar steam generation performances of plasmonic metal-based absorbers

Absorber	Evaporation rate ($kg\ m^{-2}\ h^{-1}$)	Conversion efficiency (%)	Solar density (sun)	Ref.
Au/SiO_2 core–shell NPs	—	24.0	1.4	60
Black Au membrane	0.67	42.0–57.0	1	61
Au thin film	—	44.0	1	72
Black Au film	1.51	94.5	1	75
Au/AAO	~0.95	63.9	1	76
Au/poly(*p*-phenylene benzobisoxazole) nanofibre	~1.42	83.0	1	78
Au film/airlaid paper	—	77.8	4.5	81
Au nanorods/biofoam	—	76.3	0.51	101
Au nanoflowers	2.24	90.9	1	102
Au NPs	—	58.9	3.5	100
Au/polystyrene nanofiber	1.85	98.7	1	115
Au@cellulose nanofibers	1.72	—	1	116
Au nanoflowers	~1.36	85.0	1	117
Au gyroid	1.29	74.0	1	118
Au/ceramic	1.26	87.0	1	119
Au/CuS	0.9	62.1	1	120
Au–CuS/GMs-80	1.54	88.8	1	120
Au NR@Cu_7S_4	2.35	95.5	1	121
Cu_7S_4–MoS_2–Au/PDMS	~3.82	96.6	1	122
Au@Bi_2MoO_6-carbon dots	1.69	97.1	1	123
Au/GO	1.34	84.1	1	124
Au/ZnO	0.82	—	1	125
Au@PPy/sanded cotton fabrics	1.33	~93.4	1	126
Au/PA6-GO	1.10	75.6	1	127
Au/polymeric aerogel	2.70	79.3	1	128
Black Ag nanostructure	1.32	95.2	1	74
Porous black Ag film	1.42	92.6	1	103
Ag/PPy	1.55	92.6	1	104
Ag–PSS–AG/AG	2.10	92.8	1	105
Ag@PDA	2.08	97.0	1	107
Porous polyaniline nanofibers/Ag/carbon cloth	2.21	98.0	1	129
Ag/black TiO_2/carbon porous layered foams	1.79	~81.7	1	130
Ag-BSC/bamboo shoot	1.51	86.8	1	106
TiO_2/Ag aerogel	~1.49	93.8	1	111
Polypyrrole-Ag/AgCl	1.73	95.2	1	131
Ag/PPy/poly(ionic liquid)s hydrogel	1.37	88.7	1	132
Ag/carbon cloth	1.36	92.8	1	133
Ag/$MgFe_2O_4$@surface-carbonized wood	1.55	88.6	1	134
Wood-SnS-AgNPs	1.53	90.1	1	135
Ag/GO-PW@SiO_2	1.09	95.7	1	136
Ag nanoworms-Janus membrane	~0.77	~51.1	1	137
Ag@polyacrylonitrile nanofiber membrane	1.34	76.0	1	138
Carbonized melamine foams@Ag	2.39	119.5	1	139
Bacterial cellulose/GO-Ag	2.36	94.5	1	140
AgNPs@C/melamine foam	1.62	91.3	1	141
Ag-NSP@BFP	2.77	105.2	1	142
Ag/red phosphorus	1.75	94.0	1	143
Ag/Cu_2O	1.35	~49.0	1	144
rGO/AgNPs	1.21	86.8	1	145
rGO–Ag nanowires	2.02	91.0	1	146
Ag/CuO-rGO	2.60	92.5	1	147
AgNPs@C_3N_4/GO membrane	1.13	77.3	1	148
Ag@TiO_2	~1.00	68.6	1	149
Chitosan/lignin-C@Ag aerogel	~3.57	~92.1	1	150
Ag/nanotubular TiO_2	0.82	~60.0	1	151
Ag/diatomite	1.39	92.2	1	152
Ag-PDA@wood	1.58	88.6	1	153
Cu@C/CLS	1.54	90.2	1	65
Cu/G	1.29	82.0	1	68
Cu/B–TiO_2	1.94	98.6	1	154
Cu/carbon cells	2.08	93.4	1	70
Cu@C	1.51	94.6	1	155

Table 2 (*Contd.*)

Absorber	Evaporation rate (kg m^{-2} h^{-1})	Conversion efficiency (%)	Solar density (sun)	Ref.
NC@Cu	2.76	137.1	1	71
Cu@C–N	1.94	89.4	1	156
Cu cauliflower-like nanostructure	—	>60.0	1	113
Cu NPs/cotton fabric	1.73	98.0	1	157
Cu NPs/laser-induced graphene	2.29	—	1	158
Cu NPs/C–TiO_2/SiO_2	1.50	92.2	1	159
PVA/sodium alginate–Cu–CuO_x/NC polyurethane	1.99	89.5	1	160
Cu@PPy nanowire aerogel	2.09	97.6	1	161
Plasmonic Pd/wood	1.00	68.5	1	64
Pd/sponge	2.02	131.0	1	162
Al NP/AAM	~0.92	58.0	1	66
Coral-like plasmonic black Al	2.40	166.5	1	114
Bi–C/carbon felt	1.50	91.9	1	163
Ni-NCNTs/KF	3.22	90.5	1	164
PPy@Ni sponge	1.71	85.3	1	165
Ni@C@SiO_2	1.67	91.2	1	67
Co–N–C/CF	1.88	87.0	1	166
In/microporous membrane	—	71.6	1	69
AgCu@BT/BC	1.40	95.7	1	167
Cu–Au core–shell NPs	1.02	66.0	1	36
Au/Ag-PFC fibers	1.40	86.3	1	168
Au/Ag–cellulose–polyethyleneimine	1.31	82.1	1	169
Au–Ag alloy nanocorals	2.32	64.0	1	170
Ag/Cu@sawdust biochar	1.49	90.4	1	171
Ag–Ni/cellulose	1.87	93.8	1	172
Ag/Au-GO	1.00	63.0	1	173
$Ti_3C_2T_x$/Ag@SiO_2 gel	1.42	98.0	1	174
Ag/$Ti_3C_2T_x$/ANFs	2.21	92.0	1	175
Ag–Cu-rGO	1.89	90.2	1	176

strategies have been developed to enhance the solar absorption capacity and improve the photothermal conversion efficiency of plasmonic metal NPs (Table 2).

Recently, Deng's group fabricated a self-assembled plasmonic Au thin film composed of Au NPs (diameter: ~18 nm) for solar steam generation (Fig. 5a–d).[72] This Au film exhibited broad light absorption throughout the entire visible region. By floating the Au film on the water surface to reduce heat loss, the photothermal conversion efficiency reached ~44.0% under laser irradiation at 10.18 W cm^{-2}. To further address heat loss and the limited physical stability of the Au film, they subsequently loaded the Au film onto an air-laid paper (Fig. 5e).[81] Owing to the enhanced surface roughness, improved capillary force, and low thermal conductivity of this double-layer absorber, a conversion efficiency of 77.8% was achieved under 4.5 sun irradiation. Furthermore, they studied the size-dependent effects of Au NPs on solar steam generation, observing that 10 nm Au NPs showed superior performance than their larger counterparts due to their higher absorption capability.[100] By loading 10 nm Au NPs onto highly scattering 200 nm polystyrene NPs, the system achieved a photothermal efficiency of ~58.9% under laser irradiation at 35.36 W cm^{-2}. More recently, Zhang *et al.* fabricated a self-supporting Au film with high porosity and a hierarchically porous structure by dealloying a $Cu_{99}Au_1$ precursor for solar steam generation.[75] This multiscale-structured Au film exhibited excellent hydrophilicity, broadband absorption, and efficient water transport, resulting in a water evaporation rate of 1.51 kg m^{-2} h^{-1} and a conversion efficiency of 94.5% under 1 sun irradiation. Furthermore, Zhu *et al.* developed a highly efficient, broadband plasmonic Au/anodic aluminum oxide (AAO) membrane using physical vapor deposition (PVD) (Fig. 5f–i).[76] The PVD process enabled the self-assembly of Au NPs into a thin layer on the top surface and within the inner pores of the nanoporous AAO. Owing to its high solar absorption, localized heating, and porous structure, the Au/AAO absorber achieved an evaporation rate of ~0.95 kg m^{-2} h^{-1} with the efficiency of ~63.9% under 1 sun illumination.

Additionally, numerous bio-derived and bio-inspired strategies have been developed to leverage natural structure features and their related benefits. For instance, Tian *et al.* fabricated a 3D plasmonic biofoam solar absorber by integrating Au nanorods with a biofoam (Fig. 6a).[101] This system exhibited a conversion efficiency of 76.3% under laser illumination at 5.1 W cm^{-2}, owing to its tunable LSPR wavelength, low thermal conductivity, and efficient solar absorption. Furthermore, Zhu *et al.* fabricated Au nanoflowers with broad solar absorption and outstanding photothermal effects by a tea-assisted method (Fig. 6b–f).[102] They further assembled these Au nanoflowers with polyurethane and cellulose nanocrystals, yielding a 3D porous

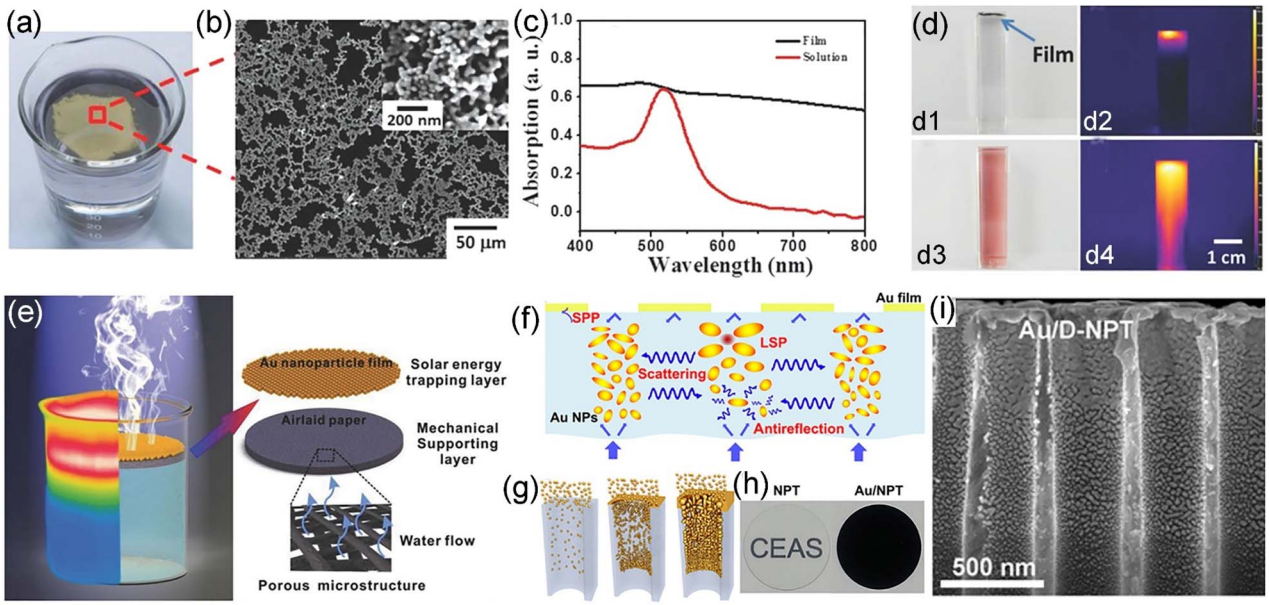

Fig. 5 (a) A photograph of a floating plasmonic Au film with a diameter >3 cm at the air–water interface. (b) Scanning electron microscopy (SEM) images of self-assembled film of Au NPs under low and high magnifications. (c) Absorption spectra of the film of Au NPs and the aqueous solution of Au NPs. (d) Optical image (d1) of an assembled Au film within a cuvette and IR side-view image (d2) of the same sample at 10.18 W cm^{-2} laser illumination. Optical image (d3) of the solution of Au NPs within a cuvette and IR side-view image (d4) of the same sample at 10.18 W cm^{-2} laser illumination. Reproduced with permission.[72] Copyright 2014, Wiley-VCH. (e) Schematic illustration of the structure of airlaid-paper-based AuNP film. Reproduced with permission.[81] Copyright 2015, Wiley-VCH. (f–i) Schematic, processes, and photographs of plasmonic Au-deposited nanoporous template (Au/NPT) absorbers. (f) Schematic of an ideal plasmonic absorber. (g) Self-assembly of Au NPs on nanoporous templates to form plasmonic absorbers. (h) Digital camera images of a 1-inch-diameter bare nanoporous template sample and a ≤90 nm thick Au/NPT sample. (i) Cross-sectional SEM image of the Au/D-NPT sample with the average pore size D ~365 nm and effective Au film thickness ~85 nm. Reproduced with permission.[76] Copyright 2016, AAAS.

solar absorber. Under 1 sun irradiation, this absorber achieved a high evaporation rate of 2.24 kg m^{-2} h^{-1} and a high photothermal efficiency of ~90.9%. Despite the fabrication of numerous plasmonic absorbers by loading plasmonic Au NPs onto various supports, the high cost of Au NPs remains a significant barrier to their widespread adoption in solar steam generation.

Owing to their more intense and localized LSPR absorption, plasmonic Ag NPs exhibited ten times more thermal generation than Au NPs.[108] Furthermore, the lower cost of Ag NPs makes them a promising alternative to Au NPs economically. Recently, various Ag-based structures have been designed and fabricated to broaden the light absorption band and improve the evaporation performance. For instance, Chen *et al.* fabricated a plasmonic black Ag nanostructure with broadband absorption by a confined seeded growth method (Fig. 7a–e).[74] Initially, Au seeds were anchored onto iron oxyhydroxide (FeOOH) nanorods within the confined space of resorcinol-formaldehyde (RF) nanoshells. Subsequently, after removing the FeOOH template, rod-shaped RF nanotubes decorated with Au seeds on their inner walls were obtained. The seeds then grew, gradually reducing interparticle spacing and enhancing plasmonic coupling, ultimately forming Ag NP assemblages with varying interparticle spacings within the tubular spaces. The interparticle coupling within these assemblages significantly enhanced plasmonic coupling, resulting in broad solar absorption. Upon 1 sun illumination, the black Ag absorber showed a water evaporation rate of ~1.32 kg m^{-2} h^{-1} with a photothermal efficiency of 95.2%. In addition, Yu *et al.* fabricated a porous black Ag film by dealloying an $Al_{99}Ag_1$ alloy (Fig. 7f).[103] This Ag film exhibited high porosity, low density, excellent hydrophilicity, and broadband solar absorption, achieving a water evaporation rate of 1.42 kg m^{-2} h^{-1} and a photothermal efficiency of 92.6%, along with high cycling stability over 30 cycles under 1 sun.

Organic polymer-polypyrrole (PPy), a photothermal organic material, shows excellent natural broadband solar absorption and high stability.[109] Furthermore, it can serve as a bridge between Ag NPs and various substrates to enhance their photothermal performance. For example, Xu *et al.* reported a photothermal absorber by coating a Ag/PPy layer onto a cellulose substrate (Fig. 7g).[104] The interwoven fibrous structure on the cellulose substrate provided interconnected channels for water transport and steam evaporation. This absorber achieved a solar absorption of 95.4%, with a water evaporation rate of 1.55 kg m^{-2} h^{-1} and a photothermal efficiency of 92.6% under 1 sun irradiation. Additionally, Sun *et al.* reported a plasmonic double-layered absorber consisting of a top layer of Ag NPs–poly(sodium-*p*-styrenesulfonate)–agarose gel (Ag–PSS–AG) and a bottom layer of agarose gel (AG) (Fig. 7h).[105] The synergetic effect between the two layers enhanced solar absorption and water transport, enabled the absorber to achieve a water

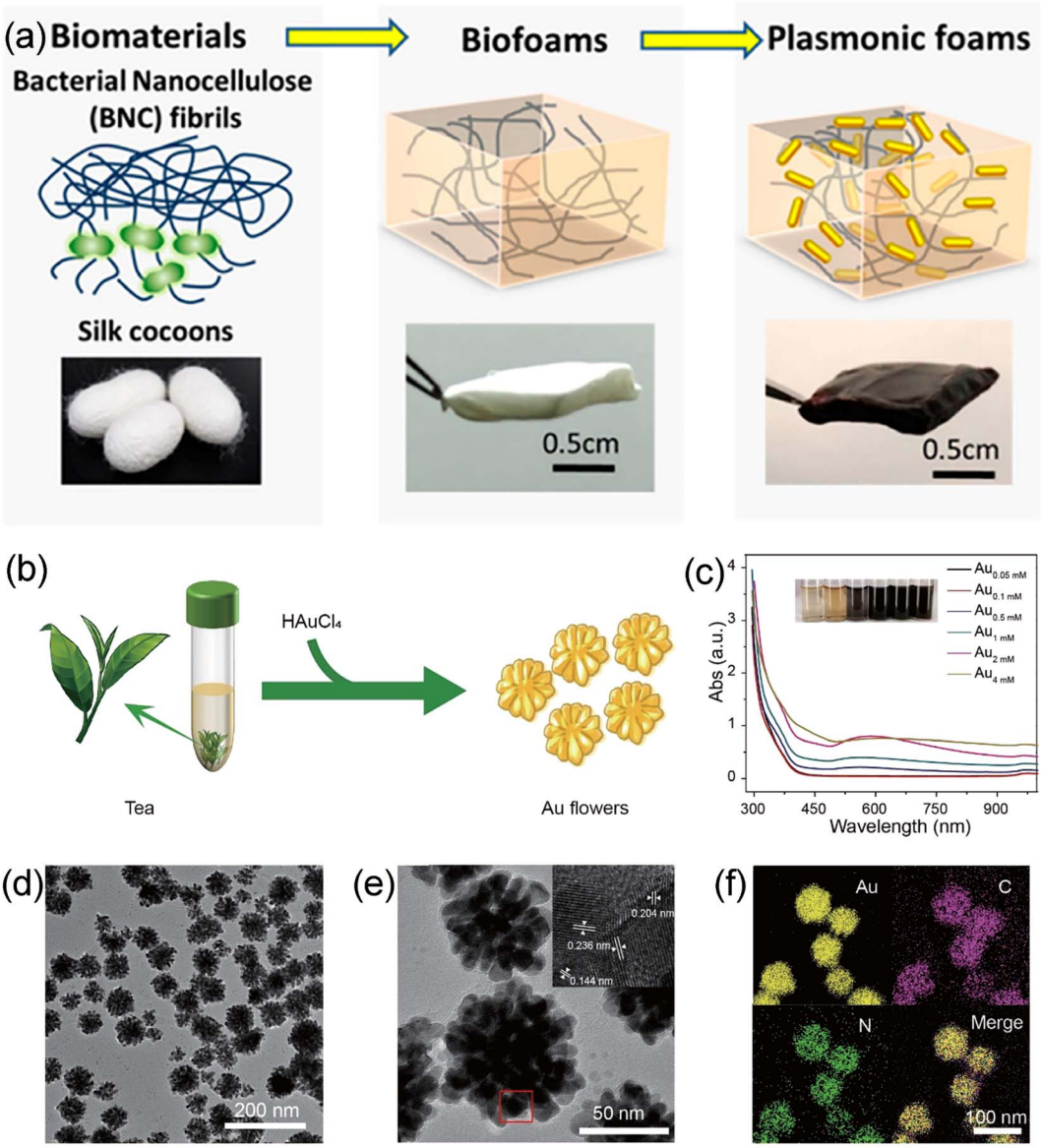

Fig. 6 (a) Schematic illustration showing the fabrication of plasmonic foams (two photographs in bottom right show the aerogel before and after dense loading of Au nanorods). Reproduced with permission.[101] Copyright 2016, American Chemical Society. (b–f) Synthesis and characterization of Au nanoflowers. (b) Schematic of Au nanoflowers synthesis. (c) UV-Vis-NIR absorption spectra of Au nanoflowers with the increasing feeding concentration of $HAuCl_4$. (d and e) Transmission electron microscopy (TEM) images of Au nanoflowers, with inset showing high-resolution TEM (HRTEM) image. (f) Elemental mapping of Au nanoflowers. Reproduced with permission.[102] Copyright 2022, Springer Nature.

evaporation rate of 2.10 kg m^{-2} h^{-1} with a photothermal efficiency of 92.8% under 1 sun.

In addition, integrating a 3D macroscopic structure with a microporous structure can effectively improve the photothermal performance.[110] For example, Gao *et al.* fabricated a 3D porous TiO_2/Ag photothermal aerogel for solar steam generation by incorporating electrospun TiO_2/Ag nanofibers into chitosan with a freeze-drying process.[111] This absorber achieved a vaporization rate of ~1.49 kg m^{-2} h^{-1} with an evaporation efficiency of 93.8% and a parallel photocatalytic hydrogen generation rate of ~3260 μmol m^{-2} h^{-1} under 1 sun, attributed to its desirable broadband absorption, aligned microchannels for mass transport, the plasmonic photothermal effect, and the confined thermal heating effect. Chen *et al.* synthesized a solar absorber composed of Ag microspheres deposited on bamboo shoot porous carbon (Ag-BSC) and bamboo shoot (Fig. 7j).[106] The Ag-BSC was fabricated *via* pyrolysis, and the double-layer solar absorber was formed by coating Ag-BSC onto a bamboo shoot. Leveraging the broadband solar absorption of Ag-BSC and the superior thermal management of bamboo shoot, the absorber achieved a water evaporation rate of 1.51 kg m^{-2} h^{-1} with a photothermal efficiency of 86.8% under 1 sun. In another study, Chen *et al.* deposited Ag@polydopamine (Ag@PDA) NPs onto a 3D porous wooden flower for solar steam generation (Fig. 7i).[107] The plasmonic-incorporated wooden flower exhibited an enhanced solar absorption of 98.65% due to the

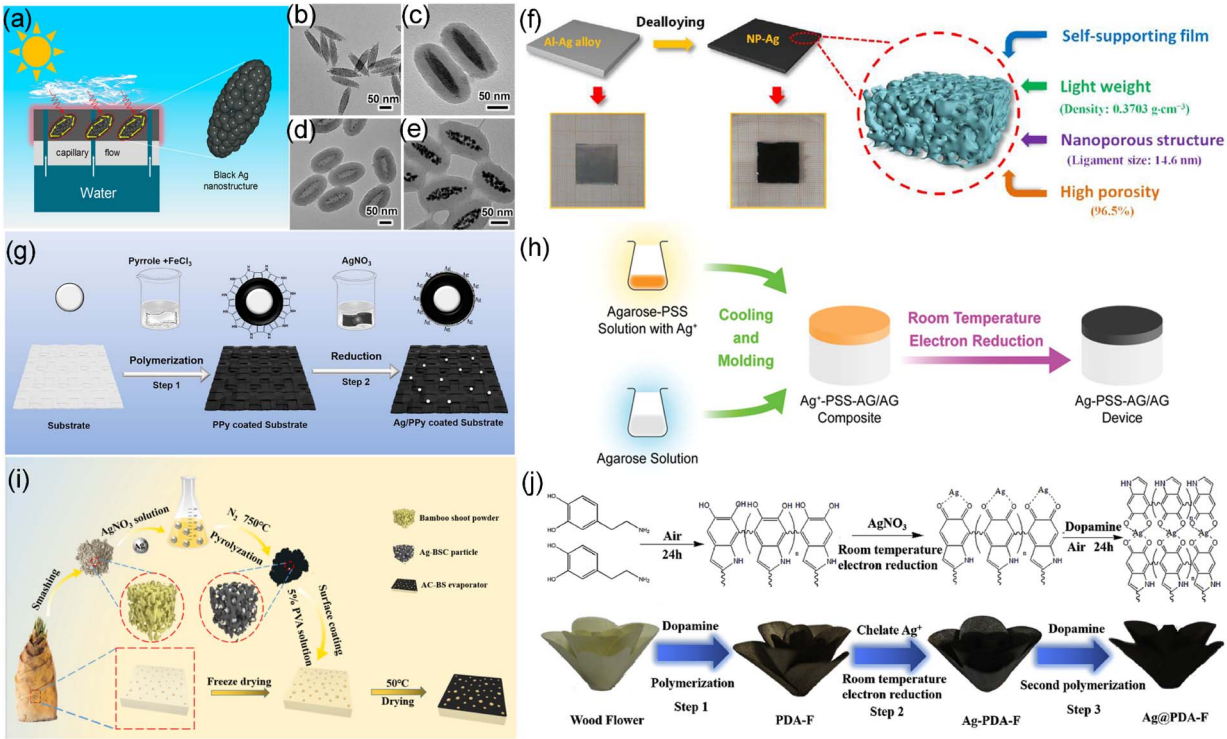

Fig. 7 (a) Space-confined seeded growth of black Ag nanostructures for solar steam generation. TEM images of (b) FeOOH nanorods with surface modified with Au seeds, (c) FeOOH/Au nanorods overcoated with a layer of RF, (d) hollow RF nanorods containing Au seeds on the inner surface prepared by removing FeOOH, and (e) RF nanorods with AgNP assemblages upon growth of Ag on Au seeds. Reproduced with permission.[74] Copyright 2019, American Chemical Society. (f) Schematic illustration showing the one-step dealloying method for preparing the NP-Ag film. Reproduced with permission.[103] Copyright 2022, Springer Nature. (g) Diagram of loading Ag/PPy on the substrate. The substrate was coated with PPy firstly, surface deposition with Ag NPs by immersing into an $AgNO_3$ solution secondly. Reproduced with permission.[104] Copyright 2019, Elsevier. (h) Fabrication procedures of Ag–PSS–AG/AG device, including agarose gelation process and silver reduction process. Reproduced with permission.[105] Copyright 2019, Wiley-VCH. (i) The fabrication process of the bamboo shoot-based bilayer evaporator. Reproduced with permission.[106] Copyright 2022, Elsevier. (j) The fabrication procedures of the plasmonic Ag@PDA wooden flower. Reproduced with permission.[107] Copyright 2020, Elsevier.

synergetic effect of plasmonic Ag@PDA NPs and the wooden flower. With abundant capillary microchannels and outstanding thermal management, the Ag@PDA absorber achieved a water evaporation rate of 2.08 kg m^{-2} h^{-1} and a photothermal efficiency of 97.0% under 1 sun. Despite the enhanced performance of plasmonic Ag-based photothermal absorbers, potential concerns regarding their poor chemical stability, toxicity and relatively high cost should be considered when plasmonic Ag NPs are applied for large-scale solar steam generation.

Cu is also an attractive plasmonic metal for solar steam generation, owing to its LSPR effect in the visible region, low cost, and high earth abundance.[112] Recently, Fan *et al.* fabricated a cauliflower-like hierarchical Cu nanostructure on a Cu surface using a laser direct writing process.[113] This nanostructure, with its broad light absorption ranging from the UV to NIR regions, achieved a photothermal efficiency of >60.0% under 1 sun. However, the poor chemical stability of Cu has greatly limited its application. To address this issue, graphene has been proven to be effective in enhancing the stability of Cu. For example, Xu *et al.* synthesized a self-floating absorber of Cu nanodot/N-doped graphene urchins (Cu/G) through a space-confined thermal treatment of Cu carbodiimide (Fig. 8a).[68] The Cu/G absorber exhibited a solar absorption of 99.0%, attributed to the intensively hybridized LSPR effect of graphene-stabilized Cu nanodots. Furthermore, the absorber showed a water evaporation rate of 1.29 kg m^{-2} h^{-1} with an efficiency of 82.0% and excellent long-term stability over 7 days under 1 sun.

More recently, core@shell structures have been shown to effectively inhibit surface oxidation and enhance the stability of Cu NPs. For example, Ren *et al.* synthesized a hybrid absorber of graphene encapsulated Cu NPs/3D carbonized loofah sponges (Cu@C/CLS) *via* a pyrolysis method (Fig. 8b).[65] The Cu@C NPs were formed *in situ* on the CLS surface *via* the pyrolysis of metal–organic frameworks and natural loofah sponges. Owing to the efficient solar absorption and local heating effect of Cu NPs, the Cu@C/CLS absorber showed a high evaporation rate of 1.54 kg m^{-2} h^{-1} and a conversion efficiency of 90.2% under 1 sun. Moreover, the ultrathin graphene provided robust protection, enabling the composite to maintain a stable evaporation performance over 7 days. In another study, Meng *et al.* synthesized a core–shell nanostructure of Cu@N-doped carbon (Cu@NC; denoted as NC@Cu in the original reference) *via* thermally treating CuO@PDA (Fig. 8c–e).[71] The Cu@NC

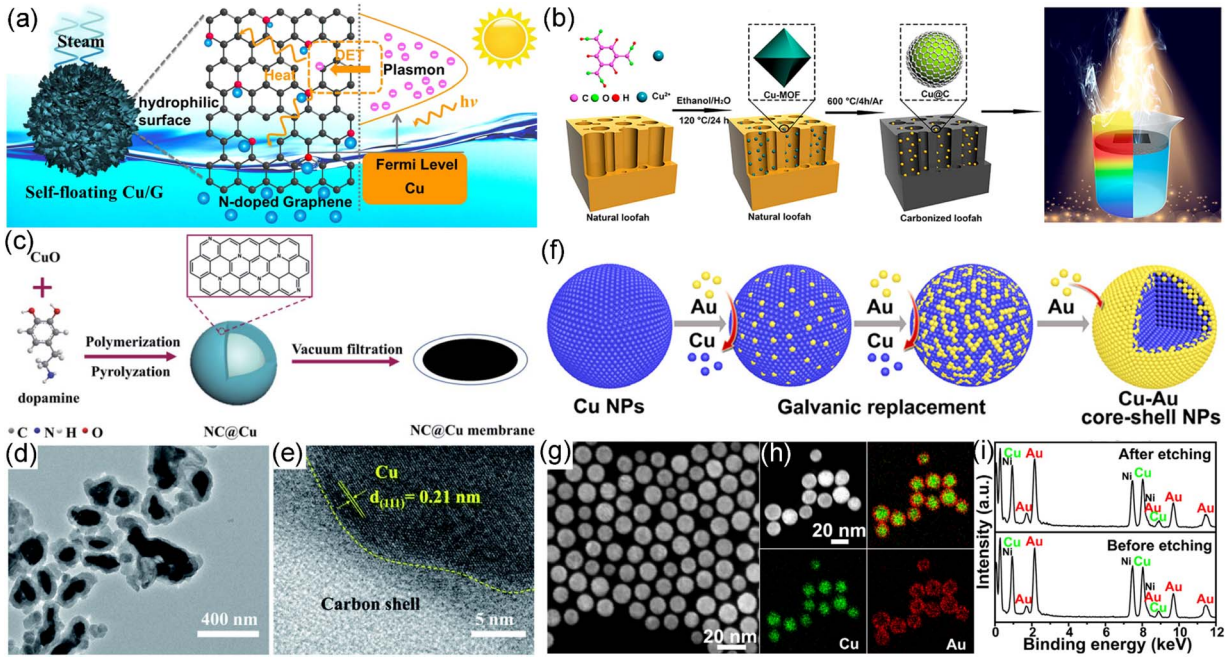

Fig. 8 (a) Schematic of the plasmon-enhanced solar desalination process: the graphene matrix serves as highway for hot electrons photoexcited by Cu LSPR and maintains the Cu surface in the metallic state. Nitrogen doping provides a hydrophilic surface which is beneficial for water infiltration and transport. While the urchin-like structure is responsible for the self-floating property, enabling the temperature increase locally at the water–air interface and thus leading to more efficient solar desalination. Reproduced with permission.[68] Copyright 2018, Elsevier. (b) Schematic illustration for the synthesis of a Cu@C/CLS structure. Reproduced with permission.[65] Copyright 2021, American Chemical Society. (c) Schematic illustration of the preparation of the Cu@NC photothermal membrane. (d) TEM and (e) HRTEM images of Cu@NC. Reproduced with permission.[71] Copyright 2022, Royal Society of Chemistry. (f) Schematic illustration of thin-shell-stabilized plasmonic Cu-based NPs. (g) High-angle annular dark-field scanning transmission electron microscopy (HAADF-STEM) image and (h) energy-dispersive X-ray spectroscopy (EDS) mapping images of $Cu_{2.5}Au_1$ NPs. (i) EDS spectra of $Cu_{2.5}Au_1$ NPs before and after the etching test with HNO_3 (1.0 M) for 30 min. Reproduced with permission.[36] Copyright 2021, American Chemical Society.

membrane exhibited high solar absorption across the full spectrum and a synergistic effect between the NC and Cu NPs, resulting in a water evaporation rate of 2.76 kg m^{-2} h^{-1} and a photothermal efficiency of 137.1% under 1 sun. This evaporation efficiency beyond the theoretical limit resulted from cold evaporation on the side surface, which lowered its temperature below ambient levels and allowed the device to draw energy from the surrounding environment. The membrane also exhibited excellent reusability during 4 days of solar desalination tests. Furthermore, our group synthesized ultrastable Cu@Au core@shell NPs through a seed-mediated process (Fig. 8f–i).[36] The Cu@Au NPs, featuring a thin and completely covered Au shell, exhibited significantly enhanced chemical stability, even in harsh environments (HNO_3 solution). Detailed characterization and analysis revealed that the external Au layer, along with its compactness and coverage, play a critical role in achieving excellent stability. Importantly, we proved that the thin Au shell has no considerable effect on plasmon dynamics and heat transfer coefficients. As a result, these Cu@Au NPs achieved a water evaporation rate of 1.02 kg m^{-2} h^{-1} and a photothermal efficiency of 66% under 1 sun, alongside high chemical stability. Despite these recent advancements in developing high-performance and stable Cu NP-based absorbers in research labs, there are still challenges in practical applications as the large-scale implementation of these core@shell NPs and long-term stability under various conditions are yet to be demonstrated.

In addition to the three most known plasmonic metals (Au, Ag, and Cu) which exhibit typical plasmon resonances in the visible range, other plasmonic metals have also been studied. For instance, Zhou *et al.* developed a photothermal absorber *via* self-assembling Al NPs within an AAO membrane (Al NP/AAM) (Fig. 9a and b).[66] This absorber showed a pronounced LSPR red shift from the UV to visible and IR regions, attributed to plasmon hybridization of close-packed NPs and surface oxidation of Al NPs. Moreover, the absorber offered unique advantages, including self-floating, broad solar absorption (>96.0%), localized heat at the water surface, and effective desalination. Under 1 sun, it achieved a water evaporation rate of ~0.92 kg m^{-2} h^{-1} and a photothermal efficiency of ~58.0%. Li *et al.* fabricated a coral-like plasmonic black Al absorber through a laser writing approach (Fig. 9c–f).[114] The laser microfabricated Al (LM Al) achieved a high solar absorption (>92.6%) and a dramatic temperature increase to >90.6 °C under 1 sun. Under solar illumination, the absorber exhibited a water evaporation rate of 2.40 kg m^{-2} h^{-1} and a photothermal efficiency of 166.5%. In another study, Zhu *et al.* reported a 3D mesoporous plasmonic wood absorber *via* decorating Pd NPs in natural wood (Fig. 9g).[64] This plasmonic wood achieved nearly full-spectrum solar absorption (≈99.0%) due to the LSPR effect of

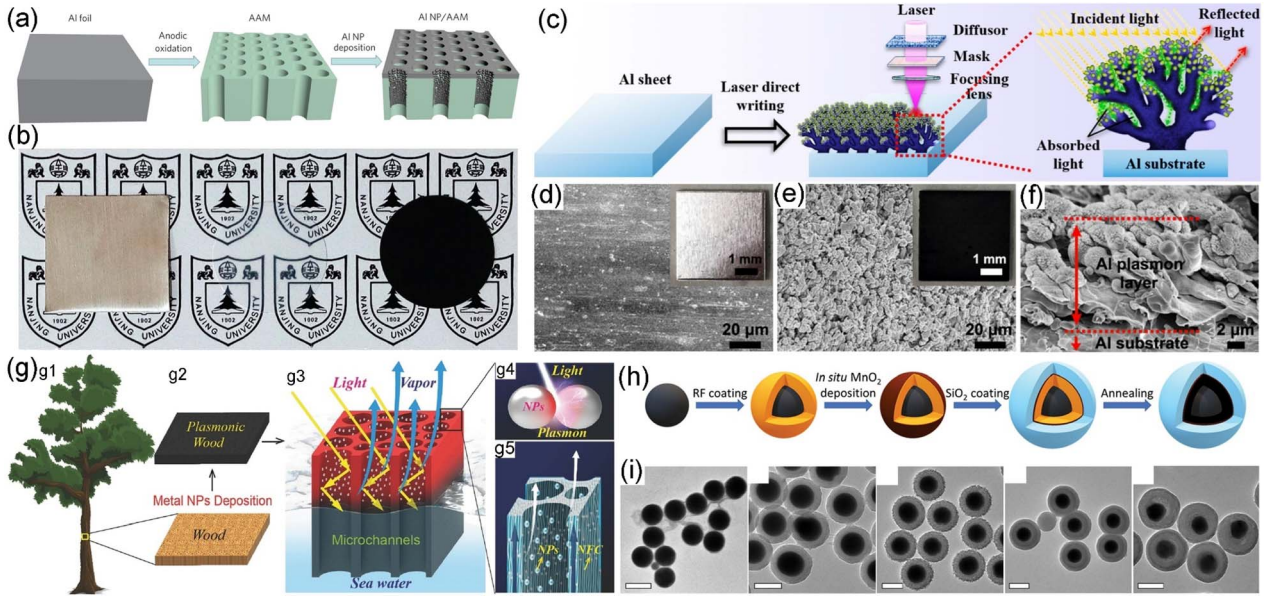

Fig. 9 (a) Fabrication of Al NP/AAM. Aluminium foils served as the source materials for the entire fabrication process, AAM fabricated by anodic oxidation, and the Al NP/AAM structure formed after the NP deposition. (b) Optical photographs of the aluminium foil, AAM sample and Al NP/AAM structure observed from the AAM side. Reproduced with permission.[66] Copyright 2016, Springer Nature. (c) Schematic of the fabrication process and solar absorption mechanism of black Al. Incident light: yellow; reflected light: red; absorbed light: green. SEM images of the surface morphologies of (d) bare and (e) LM Al surfaces. (f) SEM image of the cross-sectional view of surface micro-/nanostructures on LM Al substrate. Reproduced with permission.[114] Copyright 2021, American Chemical Society. (g) Design of plasmonic wood. (g1) A tree transports water from the bottom upward and absorbs sunlight for photosynthesis. (g2) After NP decoration, the natural wood is cut perpendicular to the growth direction of the tree and turns black due to the plasmonic effect of the metal NPs. (g3) After metal NP decoration, light can be guided into the wood lumen and be fully absorbed for steam generation. (g4) Schematic of plasmonic effect of two adjacent metal NPs. (g5) Zoomed-in schematic illustrating the water transport along microchannels in wood. The cell wall is composed of many nanofibrous cellulose (NFC). Reproduced with permission.[64] Copyright 2017, Wiley-VCH. (h) Synthetic scheme of Ni@C@SiO_2 core@shell NPs and (i) corresponding TEM images of the particles at each stage. Scale bars are all 100 nm. Reproduced with permission.[67] Copyright 2020, Wiley-VCH.

Pd NPs and the waveguide effect of natural wood. Moreover, its micro/nanochannels facilitated efficient water transport *via* capillary action. Owing to these features, the absorber exhibited a water evaporation rate of ~1.0 kg m^{-2} h^{-1} and a photothermal efficiency of ~68.5% under 1 sun. Additionally, Yang *et al.* fabricated a photothermal absorber consisting of plasmonic Ni@C@SiO_2 core–shell NPs (Fig. 9h and i).[67] Leveraging the LSPR effect of Ni NPs (around 500 nm), the broad solar absorption of C, and the protective function of SiO_2, the absorber exhibited a water evaporation rate of 1.67 kg m^{-2} h^{-1}

Table 3 Solar steam generation performances of plasmonic metal nitride-based absorbers

Absorber	Evaporation rate (kg m^{-2} h^{-1})	Efficiency (%)	Solar density (sun)	Ref.
TiN/bio-carbon foam	1.47	92.5	1	83
TiN/AAO	1.10	78.0	1	84
ZrN/AAO	1.27	88.0	1	84
HfN/AAO	1.36	95.0	1	84
TiN/ceramic fiber wool	—	80.0	1	85
TiN/AAO	—	92.0	1	86
Thermally insulated TiN/PVDF	1.34	84.5	1	87
TiN nanocavity arrays	15.00	76.0	14	88
TiN/nanoporous AAO	~1.61	87.7	1.21	89
TiN/semi-rGO	1.76	99.1	1	52
TiN/PVA	3.80	95.3	1	186
TiN@PVA/PVDF	0.94	64.1	1	182
TiN/PVDF	1.01	66.7	1	187
Porous TiN nanospheres	1.68	93.4	1	188
Hierarchical TiN nanotube mesh	3.40	~85.4	2.5	183
TiN/polyimide aerogel	2.97	94.5	1	189
MoS_2/Mo_5N_6/C-aerogel	1.89	73.3	1	190

and a photothermal efficiency of 91.2% under 1 sun. In Table 2, we have summarized various plasmonic metal-based absorbers employed in solar steam generation. However, it is important to note that the high cost, low earth abundance, and/or poor stability of these plasmonic metals present significant challenges for their practical application in solar steam generation.

4.2. Plasmonic metal nitrides

Metal nitrides (*e.g.*, TiN, ZrN, and HfN) represent another type of plasmonic photothermal materials, offering many advantages as refractory materials, including low material cost, high stability, low toxicity, and high photothermal efficiency.[177–179] Their broad LSPR arises from high electronic losses and NPs' size polydispersity. In addition, both experimental and theoretical studies have proved that metal nitrides are highly promising photothermal NMs, even better than well-established Au or Ag nanostructures due to their broadband absorption and low scattering cross-section.[180,181] Therefore, various plasmonic metal nitride-based solar absorbers with specially designed structures have been developed for solar steam generation (Table 3).

To date, plasmonic TiN nanostructures have been extensively explored for solar steam generation through integration with various supporting materials. For instance, Kaur *et al.* fabricated a plasmonic absorber by chemically immobilizing

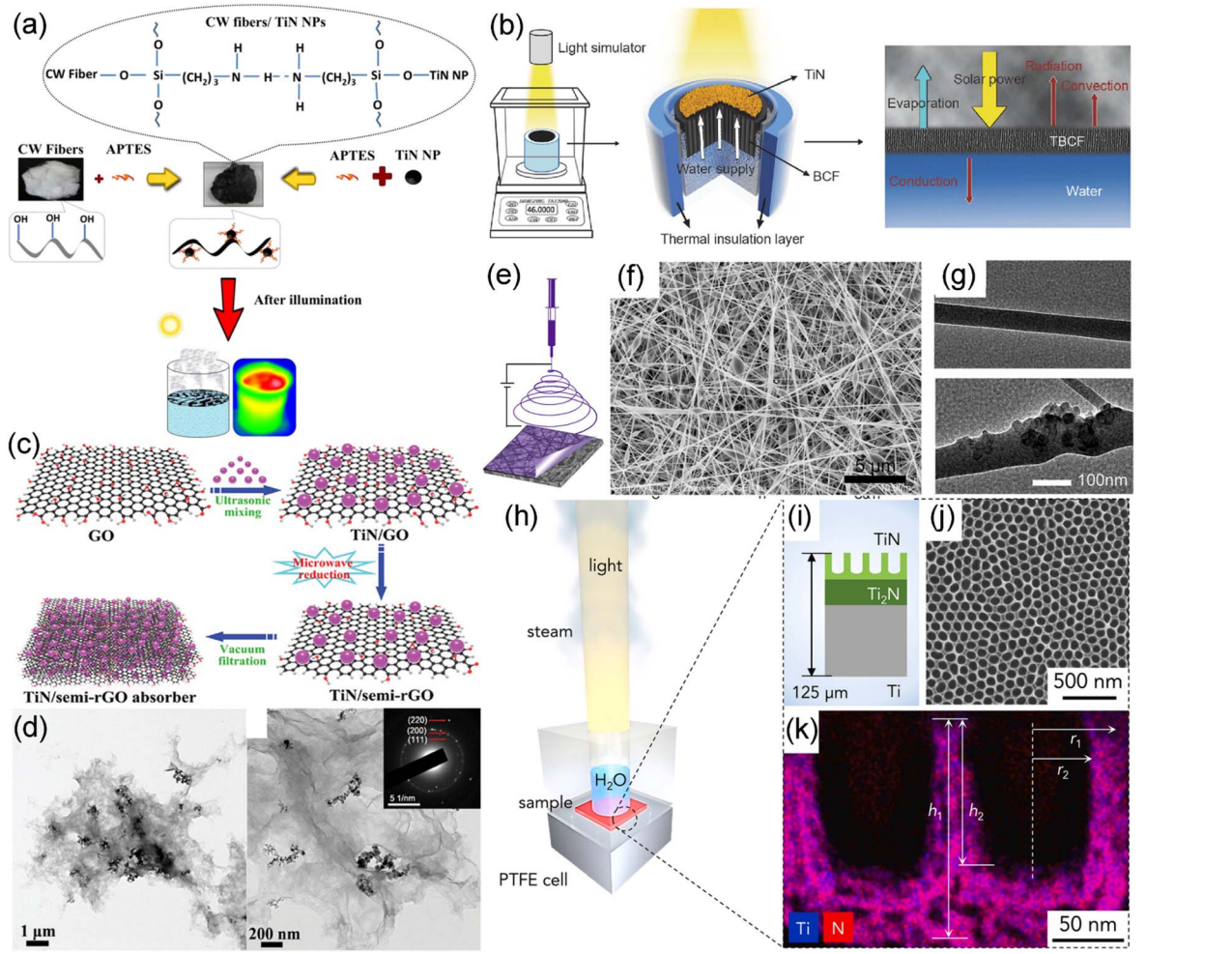

Fig. 10 (a) Schematic represents the fabrication process of TCW (TiN NPs-CW) structure with possible interactions scheme between CW fibers and TiN NPs. OH group modified CW as well as TiN NPs are functionalized with coupling agent APTES separately. TiN NPs immobilized onto TCW shows steam generation after illumination. Reproduced with permission.[85] Copyright 2017, American Chemical Society. (b) Setup for the measurement of solar water evaporation performance, schematic diagram of solar water evaporation process for the sample TBCF, and heat transfer diagram in TBCF during vapor generation process. Reproduced with permission.[83] Copyright 2018, Springer Nature. (c) Schematic illustration of the fabrication of plasmonic TiN/semi-rGO nanohybrid solar absorber. (d) TEM images of TiN/semi-rGO-25% composite at different magnifications. Inset is the corresponding selected area electron diffraction (SAED) pattern. Reproduced with permission.[52] Copyright 2023, Wiley-VCH. (e) Schematic diagram of electrospinning. (f) SEM and (g) TEM images of TiN/PVA electrospinning membrane. Reproduced with permission.[182] Copyright 2020, Elsevier. (h) Schematic of water evaporation and steam generation by the TSA (TiN-based solar absorber) under moderate light concentration in a custom-made PTFE (polytetrafluoroethylene) cell. (i) Schematic structure of the TSA: TiN nanocavities (250 nm thickness), Ti_2N thermal layer (~1 μm), and rest of the Ti substrate. (j) Top-view SEM image of TiN nanocavities. (k) HRTEM-EDS elemental mapping for Ti (blue) and N (red). Reproduced with permission.[88] Copyright 2021, Elsevier.

TiN NPs, synthesized *via* a thermal plasma method, onto ceramic fiber wool (CW) using siloxane linkages of (3-aminopropyl)triethoxysilane (APTES) (Fig. 10a).[85] Due to its broadband solar absorption, self-floating feature, and highly porous structure, the absorber containing 300 mg of TiN exhibited a photothermal efficiency of ~80.0% under 1 sun. In a later study, they also developed a solar absorber *via* loading TiN NPs onto AAO, in which the TiN NPs converted solar energy into heat and the AAO served as a water transporter.[86] By adjusting the pore diameter and TiN NP layer thickness, the TiN/AAO absorber achieved a photothermal efficiency of 92.0% under 1 sun. In addition, Guo *et al.* fabricated a porous TiN/bio-carbon foam (TBCF) absorber by depositing TiN NPs onto carbonized wood (Fig. 10b).[83] They identified an optimal absorber composition exhibiting maximal solar absorption, leading to a water evaporation rate of 1.47 kg m^{-2} h^{-1} and a photothermal efficiency of 92.5% under 1 sun. Furthermore, our group fabricated a high-efficiency plasmonic photothermal absorber consisting of TiN NPs and two-dimensional (2D) semi-rGO nanosheets by a microwave reduction method (Fig. 10c and d).[52] The semi-rGO nanosheets not only served as support materials for plasmonic TiN NPs but also enhanced water evaporation and supply. Meanwhile, the TiN NPs improved solar absorption and hydrophilicity. The layered structure of TiN/semi-rGO effectively inhibited heat loss and enhanced solar energy utilization. As a result, the evaporation rate and photothermal efficiency of the optimal absorber of TiN/semi-rGO-25% reached ~1.76 kg m^{-2} h^{-1} and 99.1% under 1 sun, respectively.

Besides inorganic materials, organic materials have also been used as supports for TiN NPs. For example, Zhang *et al.* reported a double layered TiN–poly(vinyl alcohol)/polyvinylidene fluoride (TiN–PVA/PVDF) membrane *via* an electrospinning coating and heat crosslinking process (Fig. 10e–g).[182] The TiN–PVA photothermal coating layer, consisting of PVA nanofibers with TiN nanodots, could reduce heat and mass transfer resistances because of its porous structure, interconnected pores, and good hydrophilicity. Meanwhile, the hydrophobic PVDF support effectively prevented the membrane wetting. This membrane achieved a water evaporation rate of 0.94 kg m^{-2} h^{-1} with a photothermal efficiency of 64.1% under 1 sun. In addition, modifying the structure of plasmonic TiN NMs can also improve the photothermal performance. For instance, Ren *et al.* synthesized a hierarchical TiN nanotube mesh (HTNM) *via* thermal treatment of a TiO_2 nanotube mesh, pre-prepared through electrochemical anodic oxidation of a Ti mesh.[183] They found that the solar absorption and photothermal efficiency were influenced by the thermal treatment temperature. The HTNM exhibited a water evaporation rate of ~3.40 kg m^{-2} h^{-1} with a photothermal efficiency of ~85.4% under 2.5 suns. In another study, Mascaretti *et al.* presented the scalable preparation of ultrathin TiN nanocavity arrays for solar steam generation (Fig. 10h–k).[88] By combining anodization and thermal nitridation processes, they achieved broadband solar absorption confined within the nanocavities, leveraging the plasmonic effect and cavity resonances. The plasmonic array exhibited a water evaporation rate of ~15.00 kg h^{-1} m^{-2} and a photothermal efficiency of ~76.0% under 14 suns. Despite the outstanding photothermal performance of plasmonic metal nitrides, more work is still needed to understand their stability during solar steam generation, as their plasmonic effects are highly dependent on material purity. Additionally, the synthetic processes for metal nitrides need further improvement to reduce fabrication costs and optimize the size and morphology, thereby further improving their photothermal performance. At present, TiN NMs are mainly fabricated by laser ablation[184] or direct high-temperature nitridation of TiO_2 powders,[185] which often result in broad size distribution and particle agglomeration.

4.3. Plasmonic metal chalcogenides

Plasmonic metal chalcogenides, such as $Cu_{2-x}E$ ($0 \leq x \leq 1$, where E = S, Te, and Se), are cation vacancy-doped semiconductors that show a hole concentration-dependent LSPR effect,[25] with the exception of metallic covellite CuS, where the SPR is determined by disulfide bonds. Non-stoichiometric $Cu_{2-x}E$ is a non-toxic and widely studied plasmonic semiconductor; however, its use in solar steam generation is much less than plasmonic metals (Table 4). The LSPR of $Cu_{2-x}E$ can be tuned from the NIR to mid-IR range by varying the crystal structure through changing the x value. Furthermore, varying morphology can greatly affect their photothermal conversion efficiency. Recently, Zhang *et al.* reported the synthesis of shape-controlled Cu_7S_4 nanocrystals by varying the reaction temperatures and their use in solar steam generation (Fig. 11a–c).[90] By using 1-octadecene-sulfur precursors at different reaction temperatures, Cu_7S_4 nanocrystals with disk-like and spherical morphologies were prepared. Under 1 sun, the monodisperse disk-like Cu_7S_4 nanocrystals achieved the highest photothermal conversion efficiencies of 60.5%, attributed to their strong LSPR effect. The authors also demonstrated that highly monodisperse nanocrystals had a higher water evaporation rate than polydisperse ones. In another study, Li *et al.* fabricated a photothermal absorber composed of ultralong $Cu_{2-x}S$ nanowires.[91] These nanowires, about 50 nm in diameter and tens of micrometers in length, exhibited strong solar absorption in the NIR region due to the LSPR effect. Under 1 sun, the $Cu_{2-x}S$ nanowires achieved a water evaporation rate of ~0.95 kg m^{-2} h^{-1} and a photothermal efficiency of ~66.0%. In addition, integrating plasmonic $Cu_{2-x}S$ NPs with functional supports can further improve the photothermal performance. For example, Xue *et al.* fabricated $Cu_{2-x}S$/S/rGO nanocomposites by a laser thermal method (Fig. 11d).[191] By varying the power intensity of NIR laser, the $Cu_{2-x}S$/S/rGO nanocomposite prepared at 8 W showed the strongest solar absorption due to its LSPR effect, achieving a water evaporation rate of 2.64 kg m^{-2} h^{-1} and a photothermal efficiency of ~95.6% under 1 sun.

Among various plasmonic $Cu_{2-x}S$ NMs, metallic covellite CuS exhibits a broad and strong LSPR peak in the visible and NIR regions, attributed to the high density of free holes in its valence band.[194] Unlike other plasmonic semiconductors, these free holes are primarily associated with disulfide bonds bridging CuS_4–CuS_3–CuS_4 units, rather than cation vacancies,

Table 4 Solar steam generation performances of plasmonic metal chalcogenide-based absorbers

Absorber	Evaporation rate (kg m^{-2} h^{-1})	Efficiency (%)	Solar density (sun)	Ref.
Cu_7S_4 nanocrystals	—	60.5	1	90
$Cu_{2-x}S$ nanowires	0.95	66.0	1	91
Cu_9S_5/PVDFM	~1.17	80.2	1	92
$Cu_{2-x}S$/S/rGO	2.64	~95.6	1	191
$Cu_{2-x}S$ NRs–PVA gel	1.27	87.0	1	196
MXene/Au@$Cu_{2-x}S$	2.02	96.1	1	197
CuS/polyethylene	1.02	63.9	1	93
Carbon nanoparticle/CuS/polyurethane	1.62	93.8	1	198
CuS/SCM	1.09	68.6	1	94
CuS/PVDFM	1.43	90.4	1	195
CuS hollow nanospheres	~1.30	85.1	1	199
$Cu_{2-x}Se$ NPs	1.44	~90.6	1	200
$Cu_{2-x}Se$@PDAs	2.71	—	1	192
$Cu_{2-x}Te$ nanowire	1.40	81.0	1	193

thereby allowing LSPR to be regulated by the reversible formation or cleavage of disulfide bonds without changing the composition and phase.[30] It has also attracted tremendous attention for solar steam generation. For instance, Tao *et al.* fabricated a 3D hierarchical CuS structure by a hydrothermal method.[195] When combined with a PVDF membrane support, the CuS/PVDFM absorber showed broad and high light absorption across the solar spectrum. Under 1 sun irradiation,

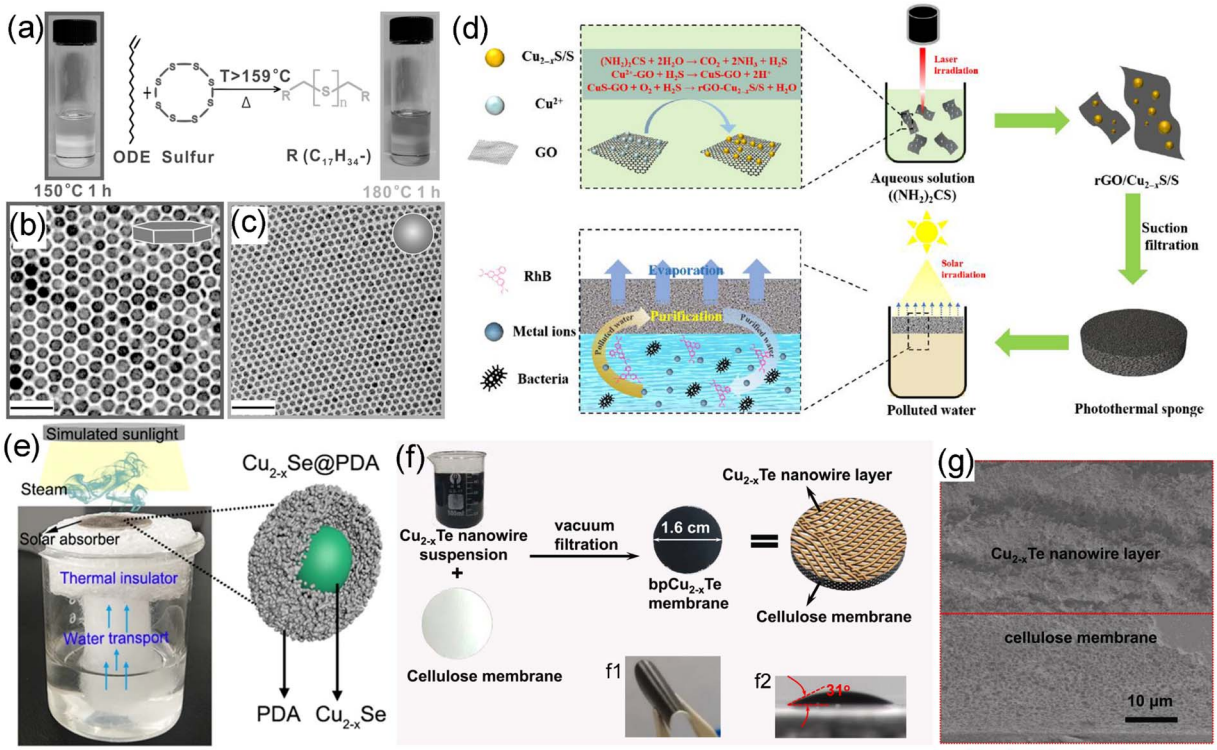

Fig. 11 (a) Schematic of reaction pathways for sulfur and 1-octadecene and colored 1-octadecene-sulfur precursor. TEM images of (b) monodisperse disk-like Cu_7S_4 nanocrystals with yellowish ODE-Sulfur precursor and (c) monodisperse spherical Cu_7S_4 nanocrystals with orange ODE-Sulfur precursor. Reproduced with permission.[90] Copyright 2016, Wiley-VCH. (d) Schematic illustrations show the laser thermal preparation of $Cu_{2-x}S$/S/rGO nanocomposites and interfacial solar water purification. Reproduced with permission.[191] Copyright 2022, Springer Nature. (e) The solar-driven evaporation device and the structure diagram of $Cu_{2-x}Se$@PDA. Reproduced with permission.[192] Copyright 2022, Springer Nature. (f) A schematic illustrating the fabrication process of the bp$Cu_{2-x}Te$ (broadband plasmonic $Cu_{2-x}Te$ nanowire) membrane. The broadband plasmonic $Cu_{2-x}Te$ nanowires are deposited onto a cellulose membrane by a vacuum filtration process, forming a double-layer structure. Insets: the inset (f1) shows a digital photograph of the bent bp$Cu_{2-x}Te$ membrane, demonstrating its robust flexibility; the inset (f2) shows a water contact angle of 31° on the bp$Cu_{2-x}Te$ membrane. (g) Representative cross-sectional SEM image of a selected area of the bp$Cu_{2-x}Te$ membrane. Reproduced with permission.[193] Copyright 2021, Elsevier.

the floatable absorber showed a water evaporation of 1.43 kg m^{-2} h^{-1} and a photothermal efficiency of 90.4%, along with excellent durability and reusability over 20 cycles. In addition, same as plasmonic $Cu_{2-x}S$ NPs, $Cu_{2-x}Se$ and $Cu_{2-x}Te$ NPs exhibited strong solar absorption and photothermal performance mainly in the NIR range. Cheng *et al.* fabricated a solar absorber composed of PDA-modified $Cu_{2-x}Se$ nanocomposites ($Cu_{2-x}Se$@PDAs) with a core@shell structure (Fig. 11e).[192] The optimal $Cu_{2-x}Se$@PDA30 absorber, benefiting from broadband absorption and efficient water transport, showed a water evaporation rate of 2.71 kg m^{-2} h^{-1} under 1 sun. In another study, Chen *et al.* reported a plasmonic $Cu_{2-x}Te$ membrane with broadband solar absorption (Fig. 11f and g).[193] This membrane presented outstanding solar absorption of ~95.9% over the full spectrum, with high porosity, excellent hydrophilicity, and low thermal conductivity, enabling a water evaporation rate of 1.40 kg m^{-2} h^{-1} and a photothermal efficiency of 81.0% under 1 sun. These studies highlight the outstanding solar absorption abilities of plasmonic metal chalcogenides, making them promising, cost-effective photothermal nanomaterials. However, further studies are needed to assess their toxicity, stability, structural composition, surface ligands, and morphological regularity. In particular, as mentioned above, the plasmonic properties of these materials are highly sensitive to charge carrier densities, which can be affected by oxidation in air or changes in surface ligands. Thus, particular attention needs to be paid to their chemical stability and interactions with their immediate environments when exploring plasmonic metal chalcogenides for plasmon-related applications.

4.4. Plasmonic metal oxides

Plasmonic metal oxides, such as MoO_3 and WO_3, have been widely developed due to their high thermal stability and their outer d-valence electronic characteristics, which enable tunable oxygen vacancy concentrations.[25] These metal oxides, with their oxygen vacancies, possess high charge carrier density, resulting in strong LSPR effects. Moreover, by adjusting the oxygen partial pressure, the number of oxygen vacancies can be easily controlled, allowing precise tuning of the LSPR peak position and intensity. This tunability makes plasmonic metal oxides very attractive for photothermal conversion application (Table 5). In addition, the introduction of oxygen vacancies leads to the emergence of defect levels and narrows the band gap, endowing broad solar absorption across the solar spectrum.[201,202]

For WO_{3-x}, by optimizing its morphology and surface nanostructures, its light-harvesting performance can be significantly enhanced. For example, Ming *et al.* synthesized 2D oxygen-deficient WO_x nanosheets by introducing oxygen vacancies into WO_3, which were used as nanofluids for solar steam generation (Fig. 12a and b).[203] Owing to the LSPR effect, the WO_x nanosheets showed broad and intense solar absorption across the entire solar spectrum. Under 1 sun, the WO_x nanofluids achieved a water evaporation rate of 1.10 kg m^{-2} h^{-1} and a photothermal efficiency of ~78.6%. In another study, Chala *et al.* fabricated a $WO_{2.72}$/polylactic acid fiber membrane *via* melt electrospinning for use as a photothermal absorber.[206] Due to its strong NIR photo-absorption and floatability on water, the fiber membrane showed a water evaporation rate of 3.81 kg m^{-2} h^{-1} and a photothermal efficiency of 81.39% under a 150 W infrared lamp. Li *et al.* developed a bilayer absorber by assembling WO_{3-x} nanorods on wood for solar steam generation (Fig. 12c–e).[96] The bilayer absorber showed a high solar absorption of ~94.0%, attributed to the broad absorption of WO_{3-x} nanorods and the multi-light scatting effect of wood pores/channels. It achieved a water evaporation rate of 1.28 kg m^{-2} h^{-1} and a photothermal efficiency of 82.5% under 1 sun. In addition, they also fabricated a 1D/2D $W_{18}O_{49}$/rGO bilayer absorber composed of $W_{18}O_{49}$ nanofibers and rGO nanosheets (Fig. 12f and g).[204] The optimized bilayer absorber achieved a water evaporation rate of 1.34 kg m^{-2} h^{-1} and a photothermal efficiency of 86.5% under 1 sun. Furthermore, Wang *et al.* fabricated a 3D hierarchical WO_{3-x}/Ni foam (WO_{3-x}/NF) absorber *via* a hydrothermal-annealing route (Fig. 12h).[205] Owing to the channel vapor escape and light-harvesting caused by the multi-scattering effect of 3D

Table 5 Solar steam generation performances of plasmonic metal oxide-based absorbers

Absorber	Evaporation rate (kg m^{-2} h^{-1})	Efficiency (%)	Solar density (sun)	Ref.
WO_{3-x} nanorods	1.28	82.5	1	96
WO_x nanosheets	1.10	78.6	1	203
$W_{18}O_{49}$/rGO	1.34	86.5	1	204
WO_{3-x}/Ni foam	1.50	88.0	1	205
$WO_{2.72}$/polylactic acid fiber	3.81	~81.4	—	206
$W_{18}O_{49}$@PDMS	1.15	80.7	1	210
$W_{18}O_{49}$ nanowires/carbon foam	~1.69	—	—	211
Cu/$W_{18}O_{49}$@graphene	1.41	88.6	1	212
WO_{3-x}/Ag/PbS/NF	1.90	94.0	1	213
MoO_{3-x} nanobelts	0.99	62.1	1	95
MoO_{3-x} nanoparticles	4.14	90.7	1	214
Flower-like MoO_x	~1.26	85.6	1	97
Nanoflower-like MoO_{3-x}	1.51	95.0	1	207
Ni-G-MoO_{3-x}	1.50	95.0	1	208
TiN/MoO_{3-x}	2.05	106.7	1	209

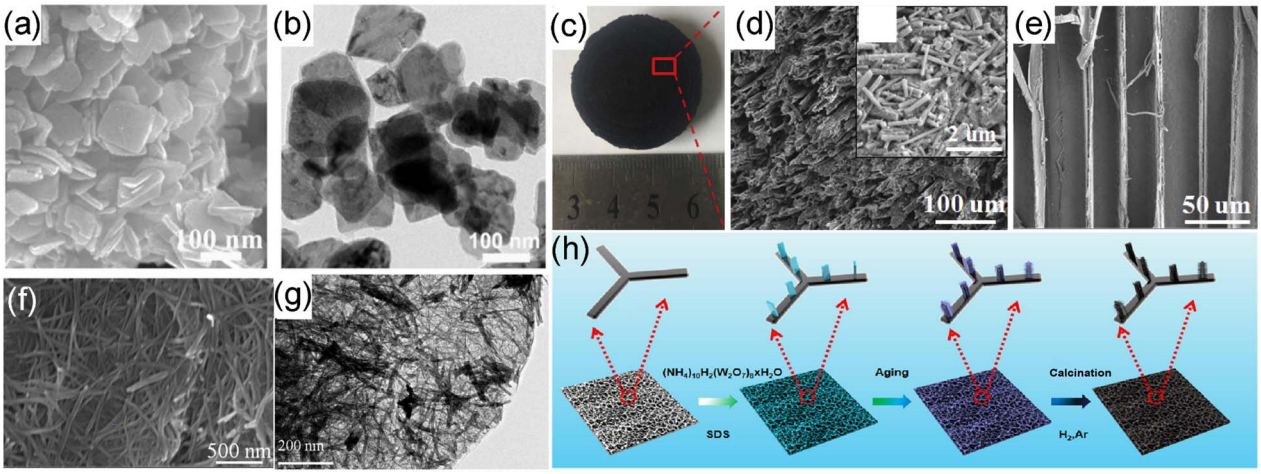

Fig. 12 (a) and (b) Structure characterization of the 2D defective WO_x ($WOAr_2$) nanosheets. (a) SEM image and (b) low-magnification TEM image. Reproduced with permission.[203] Copyright 2018, Elsevier. (c–e) Characterization of the WO_{3-x} nanorod-decorated wood evaporator. (c) The photo images of the WO_{3-x} NR-decorated wood evaporator. (d) SEM image of the wood surface and the inset shows the SEM image of WO_{3-x} nanorods on the surface of the wood. (e) SEM image of the long channels in wood. Reproduced with permission.[96] Copyright 2019, Elsevier. (f) SEM image and (g) TEM image of 1D/2D $W_{18}O_{49}$/rGO-0.01 heterostructure. Reproduced with permission.[204] Copyright 2019, Elsevier. (h) Fabrication process of the hierarchical WO_{3-x}/NF. Reproduced with permission.[205] Copyright 2021, Elsevier.

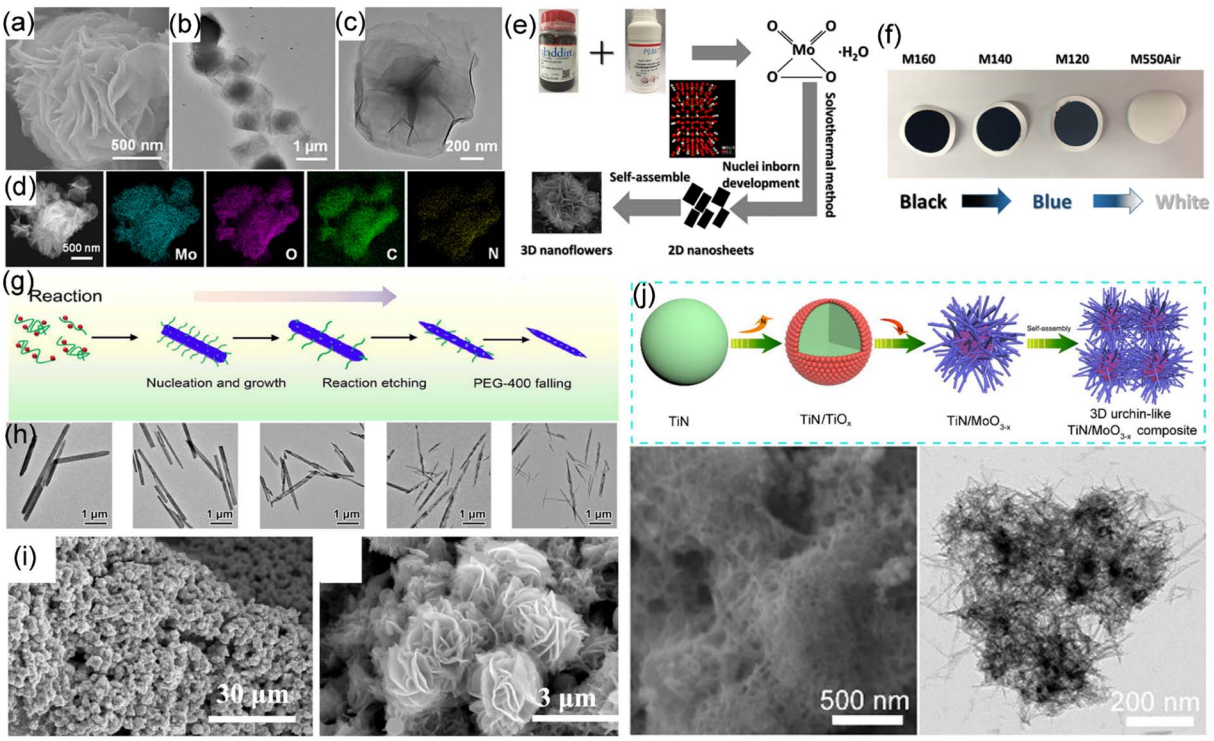

Fig. 13 (a) SEM image and (b) and (c) TEM images of the MoO_x hierarchical nanostructure. (d) Elemental mapping of the MoO_x hierarchical nanostructure. The vertical scale (bottom) is 5 nm. Reproduced with permission.[97] Copyright 2018, Wiley-VCH. (e) Schematic illustration of the fabrication process of MoO_{3-x} samples. MoO_{3-x} was prepared from Mo powder by a solvothermal method. (f) Photographs of the products synthesized at different temperatures varying from OVs (oxygen vacancies)-enriched M160 (black powder) to oxygen-recovered M550Air (white powder). Reproduced with permission.[207] Copyright 2019, Elsevier. (g) Schematic illustration of the PEG-400 surface protected reduction process for the formation of 1D MoO_{3-x} nanobelts. (h) Low-magnification TEM images of the MoO_{3-x} nanobelts synthesized in the presence of 0, 100, 200, 500 and 1000 μL of PEG-400. Reproduced with permission.[95] Copyright 2020, Springer Nature. (i) SEM images of Ni-G-MoO_{3-x}. Reproduced with permission.[208] Copyright 2021, Elsevier. (j) Schematic illustration, SEM image, and TEM image of the dual plasmonic TiN/MoO_{3-x} composite with a 3D urchin-like structure. Reproduced with permission.[209] Copyright 2024, American Chemical Society.

hierarchical porous NF and the LSPR effect of WO_{3-x}, the WO_{3-x}/NF absorber exhibited a broad solar absorption of 95.0% across the full spectrum. Under 1 sun, the WO_{3-x}/NF absorber achieved a water evaporation rate of 1.50 kg m^{-2} h^{-1} and a photothermal efficiency of ~88.0%.

Sub-stoichiometric MoO_{3-x} represents another promising class of plasmonic metal oxide for solar steam generation and has also been widely developed. For example, Lu *et al.* fabricated a flower-like oxygen-defected MoO_x hierarchical nanostructure composed of atomically thick nanosheets using a one-pot hydrothermal method for solar steam generation (Fig. 13a–d).[97] The assembled plasmonic MoO_x architecture exhibited a broad solar absorption of ~90.0%. When MoO_x was loaded onto the polytetrafluoroethylene (PTFE) membrane, the absorber achieved a water evaporation rate of ~1.26 kg m^{-2} h^{-1} with a photothermal efficiency of 85.6% under 1 sun. Huang *et al.* also synthesized a photothermal absorber of nanoflower-like plasmonic MoO_{3-x} (Fig. 13e and f).[207] The 3D MoO_{3-x} nanoflowers, benefiting from oxygen vacancy-induced LSPR effects and their flower-like structure, showed broadband solar absorption of 97.0%. As a result, the MoO_{3-x} absorber exhibited a water evaporation rate of 1.51 kg m^{-2} h^{-1} and a photothermal efficiency of 95.0% under 1 sun. In another study, Li *et al.* fabricated plasmonic MoO_{3-x} nanobelts with tunable solar absorption by the PEG-400 protected reduction method (Fig. 13g and h).[95] During synthesis, PEG-400 acted as both a reducing agent to introduce oxygen vacancies to control plasmonic absorption and a surface-protecting ligand to maintain the initial morphology of the MoO_{3-x} nanobelts. The optimal MoO_{3-x} nanobelts, with their broadband absorption and special 1D nanostructure, showed a water evaporation rate of 0.99 kg m^{-2} h^{-1} with a photothermal efficiency of 62.1% under 1 sun. Furthermore, Gong *et al.* reported a plasmonic absorber composed of graphene and MoO_{3-x} covered porous Ni (Ni-G-MoO_{3-x}) through combining chemical vapor deposition and hydrothermal methods (Fig. 13i).[208] Owing to the LSPR

Table 6 Solar steam generation performances of plasmonic MXene-based absorbers

Absorber	Evaporation rate (kg m^{-2} h^{-1})	Efficiency (%)	Solar density (sun)	Ref.
$Ti_3C_2T_x$/PANI	2.65	93.7	1	218
PDA@$Ti_3C_2T_x$	~1.28	85.2	1	217
$Ti_3C_2T_x$–TiO_X	2.09	92.0	1	221
$Ti_3C_2T_x$/polyethyleneimine/PDA/melamine foam	1.47	88.7	1	222
$Ti_3C_2T_x$ anchored structure	2.48	89.3	1	223
$Ti_3C_2T_x$/FCuS	1.34	93.0	1	224
$Ti_3C_2T_x$/carbon nanotube	2.10	93.4	1	225
$Ti_3C_2T_x$/rGO hydrogel	3.62	91.0	1	219
$Ti_3C_2T_x$/cellulose	1.44	85.8	1	226
$Ti_3C_2T_x$ nanoflakes/copper indium selenide	1.43	~90.0	1	227
MXene/PDA@TiO_2/Fe_3O_4@C22-HMC	2.09	94.4	1	228
HAP/PDA-modified $Ti_3C_2T_x$/PAM/PVA aerogel	2.62	93.6	1	220
Carbonized MXene/PDA foam	~1.60	89.8	1	229
$Ti_3C_2T_x$/diatomite-modified coconut husk	2.10	~90.6	1	230
GO/$Ti_3C_2T_x$ aerogel	1.27	90.7	1	231
Aligned reduced graphene oxide/$Ti_3C_2T_x$	2.09	93.5	1	232
$Ti_3C_2T_x$/rGO/MoS_2	1.33	90.1	1	233
MoS_2/Ti_3C_2 aerogel	2.75	—	1	234
Ti_3C_2–MnO_2@luffa sponge	1.36	~85.3	1	235
Cu_3BiS_3/Ti_3C_2	1.32	91.9	1	236
Chitosan-Ti_3C_2-PDA-Ag	2.31	90.8	1	237
$Ti_3C_2T_x$AuNFs	1.59	97.8	1	238
Porphyrin-$Ti_3C_2T_x$	1.41	86.4	1	239
SiO_2/$Ti_3C_2T_X$/poly(tetrafluoroethylene)	1.53	85.6	1	240
Poly(lactic acid)/$Ti_3C_2T_x$@MoS_2	1.39	91.0	1	241
Chitosan/lignin aerogel-carbonized lignin@MXene	2.35	88.2	1	242
MXene/cellulose composite cloth	1.34	89.6	1	243
$Ti_3C_2T_x$/aramid nanofiber aerogels	1.48	93.8	1	244
Ti_3C_2/wood aerogel	2.00	92.6	1	245
$Ti_3C_2T_X$/carbon aerogels	1.48	92.3	1	246
$Ti_3C_2T_X$/cellulose nanofibers/luffa aerogels	1.40	91.2	1	247
$Ti_3C_2T_x$/Au@$Cu_{2-x}S$	2.02	96.1	1	197
$Ti_3C_2T_x$/$La_{0.5}Sr_{0.5}CoO_3$	2.26	92.3	1	248
Perovskite/Ti_3C_2/PVA hydrogels	1.98	90.0	1	249
Foamy Ti_3C_2 membrane	1.54	87.1	1	250
$Ti_3C_2T_x$-based hydrogel-coated cotton fabrics	1.65	95.0	1	251
PVA/$Ti_3C_2T_x$/p-g-C_3N_4	1.85	93.5	1	252
$Ti_3C_2T_x$ flexible Janus membrane	1.34	81.5	1	253
PPy/$Ti_3C_2T_x$-PDA-fabric	~1.49	90.6	1	254

effect of plasmonic MoO_{3-x}, the absorber exhibited improved solar absorption (96.0%). The Ni-G-MoO_{3-x} absorber, with its superhydrophilic solar absorbing layer, showed a water evaporation rate of 1.50 kg m^{-2} h^{-1} with a photothermal efficiency of 95.0% under 1 sun. Recently, our group developed a 3D dual plasmonic TiN/MoO_{3-x} composite as a photothermal absorber for solar steam generation (Fig. 13j).[209] This 3D composite features a biomimetic urchin-like structure composed of plasmonic TiN NPs and MoO_{3-x} nanorods. Owing to its high hydrophilicity, efficient water transport, high surface area, and potential multiple light scattering effects, the composite absorber achieved a water evaporation rate of ~2.05 kg m^{-2} h^{-1} and a photothermal efficiency of 106.7% under 1 sun. The dual plasmonic nanostructure and photothermal stability of this composite were further demonstrated using photon-induced near-field electron microscopy combined with electron energy-loss spectroscopy and advanced *in situ* laser-heating TEM, respectively. Although plasmonic oxygen-deficient metal oxides exhibit outstanding solar absorption, their photothermal performance can be further improved by regulating their morphology, size, and composition.

4.5. Plasmonic MXenes

Plasmonic MXenes are 2D nanomaterials composed of transition metal carbides/nitrides, with the chemical formula $M_{n+1}X_nT_x$ (n = 1–3), where M, X, and T present early transition metals (most commonly, Ti), C and/or N, and surface functional groups (such as –O, –OH and –F), respectively. The favorable features of MXenes include high mechanical stiffness, excellent photothermal conversion efficiency, tunable surface chemistry, and excellent high hydrophilicity, making them ideal candidates for solar steam generation.[98,215] In particular, $Ti_3C_2T_x$, the first synthesized MXene, has been widely investigated in solar steam generation. Its typical synthesis involves selective etching of its parent $M_{n+1}AX_n$ phases (A is an A-group element), known as MAX, with hydrofluoric acid or fluoride salts and exfoliation to form 2D sheet-like structures.[216] They have been combined with other materials, such as plasmonic metals, semiconductors, carbon-based materials, organic polymers, to form MXene-based composites in various forms, including films, aerogels, hydrogels, and fabrics. Forming these composites significantly improved the solar absorption and water evaporation rate because of their plasmonic photothermal effect and structural properties (Table 6).

Recently, the integration of plasmonic MXenes with organic polymers to form MXene-based composites has been widely reported. For instance, Zhao *et al.* synthesized PDA@MXene microspheres for solar steam generation *via* a hydrogen bond-induced self-assembly method (Fig. 14a).[217] By combining PDA, known for its excellent light absorption, with plasmonic $Ti_3C_2T_x$ MXene, the PDA@MXene microspheres achieved a synergistic solar absorption capacity of ≈96% in the range of 250–1500 nm.

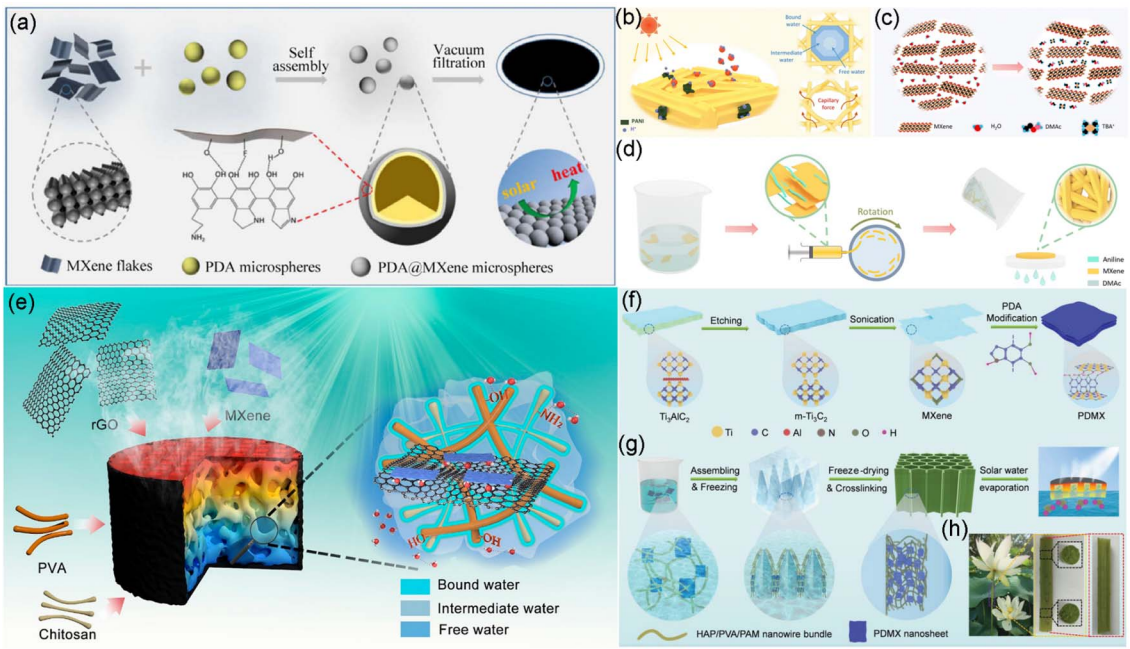

Fig. 14 (a) Schematic illustration for the fabrication of the PDA@MXene photothermal layer. Reproduced with permission.[217] Copyright 2020, Springer Nature. (b) Schematic illustration of interfacial solar vapor evaporation of MXene/PANI fabrics. (c) Solvent exchange process for obtaining $Ti_3C_2T_x$ organic solvent dispersion. (d) Schematic illustration of preparation of MPs. Reproduced with permission.[218] Copyright 2023, Royal Society of Chemistry. (e) Schematic illustration of the SSG (solar steam generation) technology caused by the synergy of tailored water states in confined space and concave pyramid-shaped surface topography of $Ti_3C_2T_x$ MXene/rGO-embedded hybrid hydrogels. Reproduced with permission.[219] Copyright 2021, American Chemical Society. (f) The preparation and surface modification of MXene nanosheets with *in situ* polymerized PDA molecules. (g) Fabrication of the biomimetic PDMX/HPP aerogel with vertically aligned channels for solar energy-driven water evaporation. (h) Digital images of the lotus stem, and the transverse and longitudinal directions of the lotus stem. Reproduced with permission.[220] Copyright 2023, Wiley-VCH.

Moreover, the excellent hydrophilicity of the microspheres is conducive to rapid water transport and vapor escape. As a photothermal film, the PDA@MXene microspheres exhibited a water evaporation rate of ~1.28 kg m^{-2} h^{-1} and a photothermal efficiency of 85.2% under 1 sun. In another study, Ding *et al.* combined plasmonic MXene with a photothermal polymer of polyaniline (PANI) to fabricate MXene/PANI non-woven fabrics (MPs) by a wet-spinning process (Fig. 14b–d).[218] The porous structure and crumpled micro-surface of the MXene/PANI fabrics enabled a high water evaporation rate of 2.65 kg m^{-2} h^{-1} and a photothermal efficiency of 93.7% under 1 sun.

Furthermore, Lu *et al.* designed a hybrid hydrogel embedded with 2D nanostructures for solar steam generation by simultaneously infiltrating $Ti_3C_2T_x$ and rGO nanosheets into a polymer network composed of PVA and chitosan (Fig. 14e).[219] The fabricated $Ti_3C_2T_x$/rGO hydrogel absorber, featuring surface patterns, reduced the evaporation enthalpy and induced a Marangoni effect, achieving a water evaporation rate of 3.62 kg m^{-2} h^{-1} and a photothermal efficiency of 91% under 1 sun. In another study, Wang *et al.* fabricated a lotus-stem-inspired hydroxyapatite (HAP) nanowires/PDA-modified $Ti_3C_2T_x$ MXene/polyacrylamide (PAM)/PVA aerogel (PDMX/HPP) with vertically aligned channels for solar steam generation (Fig. 14f and g).[220] Benefiting from the vertically arranged pore structure of ~20–70 μm diameter, excellent mechanical properties, outstanding hydrophilicity and water transport, strong water absorption capacity and reduced evaporation enthalpy, the aerogel achieved a water evaporation rate of 2.62 kg m^{-2} h^{-1} with a photothermal efficiency of 93.6% under 1 sun.

However, in general, plasmonic MXenes face several challenges. First, their synthesis typically involves complex processes and the use of hazardous chemicals, which poses challenges in large-scale practical applications. Second, MXenes have poor stability and are prone to corrosion and oxidation, further limiting their practical applications. Specifically, for solar steam generation, the strong interlayer interactions inherent to the 2D structure of MXenes make it difficult for them to maintain monodispersity, thereby compromising their photothermal performance. Therefore, improving the colloidal and chemical stability of 2D MXenes is a key challenge to advance their practical applications.

5. Applications of plasmonic photothermal NMs in solar steam generation

Extensive research on plasmonic photothermal NMs for solar steam generation has opened up numerous opportunities to advance their practical applications.[255] In this section, we highlight several most promising applications, including seawater desalination, sewage treatment, electricity generation, and sterilization.

5.1. Seawater desalination

Solar seawater desalination has received extensive attention as a promising technology to address global freshwater shortages. On one hand, it effectively reduces the concentrations of ions such as Na^+, K^+, Ca^{2+}, B^{3+}, and Mg^{2+} in seawater, enabling the produced water to meet drinking water standards set by the World Health Organization (WHO) and the US Environmental Protection Agency (EPA).[256] On the other hand, it facilitates the accumulation and collection of salt, offering potential economic benefits.[257] Recently, the efficiency of solar seawater desalination has been greatly improved by using plasmonic photothermal NMs for solar steam generation. For instance, Zhou *et al.* employed a plasmonic Al NP/AAM membrane as a plasmon-enhanced solar desalination absorber.[66] Fig. 15a presents the schematic of a solar seawater desalination device. Under solar irradiation, steam generated by the absorber continuously condenses within the device chamber. The absorber significantly reduced the salinity of seawater from various regions to meet drinking water standards (Fig. 15b). Furthermore, the concentrations of Na^+, K^+, Mg^{2+}, B^{3+}, and Ca^{2+} ions were largely reduced, falling below levels achieved by membrane- and distillation-based desalination methods (Fig. 15c). Despite the rapid development of numerous plasmonic photothermal absorbers for desalination, salt crystallization and accumulation during operation can significantly reduce solar absorption and block the pore structures of solar absorbers, negatively impacting evaporation rates and increasing operational costs. Therefore, designing plasmon-driven solar seawater desalination systems with self-cleaning capabilities and anti-salt rejection structures is crucial to ensure long-term durability and high efficiency.

5.2. Sewage treatment

Solar steam generation for domestic and industrial sewage treatment represents another significant application, offering a dual benefit of alleviating drinking water shortages and mitigating environment pollution. Recently, the removal of heavy metal ions, bacteria (*e.g.*, *E. coli* and *S. aureus*), and organic dyes (*e.g.*, methylene orange, rhodamine B, and methylene blue) by plasmon-driven photothermal solar steam generation has been extensively studied.[52,65,70,128,176] For example, Tian *et al.* developed a sandwich hydrogel ($L_{2.5}$-$Cu_{1.0}$-PC) solar absorber composed of plasmonic Cu/carbon cells for sewage treatment.[70] It could remove the concentrations of heavy metal ions (Cr^{3+}, Cd^{2+}, Zn^{2+}, Ni^{2+} and Cu^{2+}) by up to six orders of magnitude, leading to "safe" concentrations below 0.01 mg kg^{-1}, which meets drinking water standards (Fig. 15d). Moreover, the $L_{2.5}$-$Cu_{1.0}$-PC hydrogel also exhibited outstanding antibacterial effect on typical *E. coli* and *S. aureus*. In another study, Ren *et al.* used the Cu@C/CLS absorber to purify sewage containing organic dyes.[65] The absorber exhibited an ultra-high rejection rate of nearly 100% for methylene blue and methyl orange dyes (Fig. 15e). Furthermore, the plasmonic solar absorbers with photocatalytic functionality have also been employed for the solar purification of industrial sewage containing volatile organic compounds (VOCs), effectively degrading organic pollutant molecules in distilled water.[258] Therefore, the development of multifunctional plasmonic photothermal NMs for sewage treatment holds great potential for enhancing

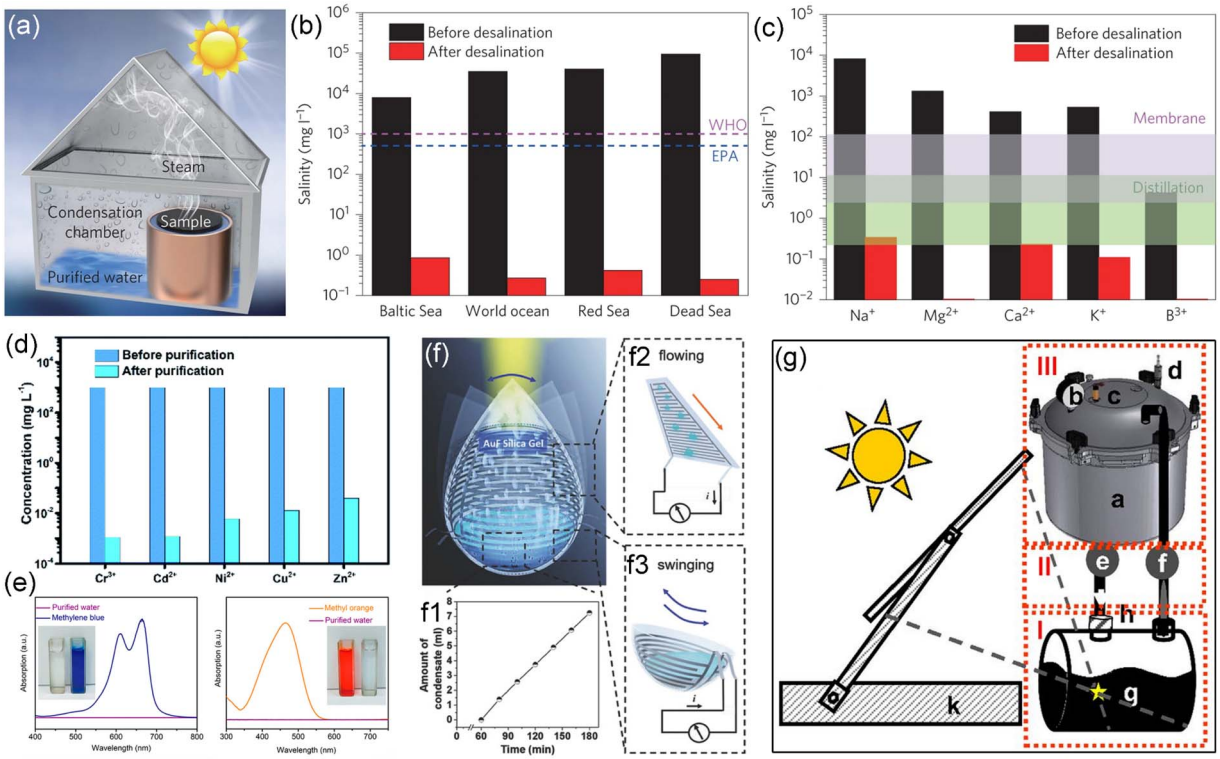

Fig. 15 (a) Experimental setup for solar desalination. (b) The measured salinities (the weight percentage of Na^+) of the four simulated seawater samples before and after desalination. (c) The measured concentrations of four primary ions in an actual seawater sample before and after desalination. The purple (green) shaded area refers to the overall typical salinity achieved by traditional membrane (distillation) desalination process, respectively. Reproduced with permission.[66] Copyright 2016, Springer Nature. (d) The overall heavy metal ions removal performance of the $L_{2.5}$-$Cu_{1.0}$-PC hydrogel before and after solar distillation (including the contribution from adsorption). Reproduced with permission.[70] Copyright 2021, Royal Society of Chemistry. (e) Model water purification performance of a Cu@C/CLS device. Absorption spectra of methylene blue solution and methyl orange solution before purification and the corresponding condensed water after purification. Reproduced with permission.[65] Copyright 2021, American Chemical Society. (f) Schematic diagram of the integral prototype for condensate collection and triboelectric energy generation. (f1) The condensate collected under focused sunlight after the first 60 min. Schematic diagram of triboelectric nanogenerator (TENG) for (f2) water flowing down the wall and (f3) water swinging in the round bottom vessel. Reproduced with permission.[117] Copyright 2018, Wiley-VCH. (g) Schematic of the closed-loop solar autoclave showing (I) the steam generation module, (II) the connection module, and (III) the sterilization module. Reproduced with permission.[99] Copyright 2013, PNAS.

purification performance and contributing to environmental remediation.

5.3. Electricity generation

The conversion of solar energy into electricity *via* photovoltaic, photochemical, and photoelectric methods has been extensively explored, given the abundance of solar energy and the growing global energy demand.[256] Integrating plasmon-driven solar steam generation with electricity generation has also been proposed using various strategies.[136,259] For example, Gao *et al.* designed a solar device containing a plasmonic Au nanoflowers/porous silica gel absorber and a PTFE film to collect evaporated water molecules and generate electricity through triboelectric effects (Fig. 15f).[117] The generated steam condensed into water droplets on the inner wall, which then flowed downward for collection. Owing to the contact of water with the PTFE film, the PTFE surface became negatively charged. When positively charged water droplets flowed across multiple individual electrodes, they induced more negative charges on the electrodes, creating a potential difference between them. Since the round bottom of the device is easily swayed by wind, the motion of collected water at the bottom creates continuous triboelectricity. The plasmonic device can generate electrical outputs up to ~0.63 μW. In addition, Ibrahim's group used plasmonic AgCu/sawdust-derived biochar@PVA and AuCu/rGO absorbers for simultaneous solar steam generation and thermoelectricity generation.[171,176] Leveraging the Seebeck effect, the temperature difference produced under solar illumination enabled both steam generation and electricity production. These plasmonic absorbers reached power densities of 34.7 mW m^{-2} and 5.72 W m^{-2} under 1 sun. These innovative strategies offer promising solutions to tackling the pressing energy and environmental challenges.

5.4. Sterilization

Traditional medical sterilization processes typically require high-temperature (>121 °C) and high-pressure (>205 kPa) saturated steam. With advancements in solar steam generation

technology, solar steam sterilization has emerged as a cost-effective and rapid alternative to eliminate bacteria and other microorganisms under light irradiation. For example, Zhang *et al.* designed a solar steam sterilization system using a rGO/PTFE composite membrane as the photothermal material. This system achieved a steam temperature exceeding 132 °C under a solar power density of 2.56 W cm^{-2}, resulting in a sterilization time of less than 5 min and a solar conversion efficiency of 84%.[260] Plasmonic materials have also been explored for solar steam sterilization. Neumann *et al.* employed broadband light-absorbing nanofluids composed of Au nanoshells as photothermal materials for solar steam sterilization (Fig. 15g).[99] Their design of an efficient solar autoclave, enabled by solar steam generation, significantly shortened the sterilization cycle time (from 15 min at 121 °C to 5 min at 132 °C). Recently, Saleque *et al.* developed a plasmon-driven solar steam sterilization system, employing a 1D–2D metallic MWCNTs and $HfTe_2$ van der Waals heterostructure as the photothermal material.[261] The 1D metallic MWCNTs leveraged LSPR to confine heat in a small area, achieving a steam temperature of 132 °C in 20 min and a water evaporation efficiency of 87.43% under 1 sun illumination. Moreover, their designed sterilization device caused a 99.04% reduction of *E. coli* bacteria after 30 min, exceeding the sterilization requirements of WHO. Despite the significant progress in plasmon-driven solar steam sterilization, several challenges remain yet. These include the need for low-cost materials and solar steam sterilization reactor designs that are suitable for real-world applications.

6. Conclusion and outlook

Solar steam generation is widely considered as a cost-effective and promising strategy for freshwater production. In this review, we have summarized recent advances over the past decade in plasmonic photothermal NMs, such as metals, metal nitrides, metal chalcogenides, metal oxides and MXenes, for solar steam generation. Among these plasmonic absorbers, overall metal nitride- and MXene-based NMs are particularly promising and attractive, as they often provide a better trade-off between efficiency, cost, stability, and scalability. By comparing the water evaporation rates and photothermal conversion efficiencies of these plasmonic NMs, we aim to clarify key directions for their future development. Although numerous strategies have been explored to enhance the solar steam generation performance and economic viability *via* broadening and enhancing solar absorption, optimizing thermal management, reducing costs, and enhancing stability, several problems remain to be solved so as to eventually realize efficient, low-cost, and stable plasmonic photothermal NMs that can fully realize their practical potential.

Firstly, the high cost (*e.g.*, materials and fabrication) and/or limited stability of plasmonic NMs greatly hinder their large-scale practical applications. Plasmonic photothermal NMs are highly attractive owing to their unique and strong light–matter interactions and localized electromagnetic fields. However, to enable a viable technology, they must exhibit robust, long-term chemical and physical stability; otherwise, performance degradation will take place unexpectedly, which is extremely detrimental to large-scale processes such as desalination or wastewater treatment. Regarding synthesis, the complicated preparation processes and the need for tightly controlled reaction conditions seriously restrict synthesis scalability. For example, we successfully synthesized highly stable laboratory-grade plasmonic Cu@Au NPs under a nitrogen atmosphere by precisely controlling the reaction conditions. However, attempts to scale up the synthesis resulted in NPs with poor uniformity and low yield. Achieving large-scale production of such NPs without compromising their structure and properties remains a great challenge. Since cost-effective materials and fabrication, scalable production and high stability have always been the essential prerequisites for widespread implementation, considerable efforts are required to address these issues.

Secondly, the integration of plasmonic and carbon-based photothermal materials offers a promising avenue to further improve solar steam generation performance. Carbon-based materials, derived from natural sources (*e.g.*, wood) or synthetic sources (*e.g.*, polymers), have been widely employed in solar steam generation due to their numerous advantages, including excellent solar absorption, low cost, high stability, lightweight characteristics and porous structures. The porous nature of these materials enhances solar absorption by plasmonic NPs or carbon materials through multiple light scattering events, meanwhile facilitating efficient water transport to the absorber surface. Combining plasmonic NPs with carbon-based materials not only enhances the solar absorption capacity and photothermal efficiency but also reduces costs, as the porous structure enables uniform dispersion of plasmonic NPs on the substrate, thereby increasing their utilization efficiency. Therefore, the key to advancing photothermal performance lies in the effective and robust integration of two exceptional photothermal materials.

Thirdly, the rational structural design of plasmonic NMs is crucial for achieving superior photothermal performance. As discussed above, the photothermal conversion efficiency highly relies on the SPR properties. Various morphologies, such as nanospheres, nanorods, nanowires, nanoflowers, and nanosheets, have been developed to tailor their SPR behavior. Among these, spherical-shaped NPs have been found to be the most effective in photothermal conversion, and further, their assembly often leads to even higher performance. How can the correlation of their delicate structural features with SPR properties contribute to future structural design? What synthetic and assembly routes need to be further developed towards the final goal? How to maximize the benefits from plasmonic NPs with as least as possible expensive materials? Significant efforts are required to address these questions, which can offer valuable insights. Although some fundamental understanding of plasmonic photothermal phenomena has been gained, current knowledge is still limited. Theoretical simulations and machine learning are expected to provide valuable guidance for accelerating future research in this field.

Finally, systematic theoretical and experimental investigations need to be closely integrated to comprehensively understand the influence of solar absorbers on the solar steam

generation performance. These investigations should include not only light absorption ability, evaporation rate, and water supply efficiency but also thermal management, taking into consideration downward heat conduction losses, radiation losses to the surroundings, and convective heat losses. Experimental data should be fed back into the design loop and theoretical models timely modified. Additionally, environmental factors such as temperature, humidity, and wind speed interference also affect the evaporation performance and long-term stability of solar absorbers. By gaining a deeper understanding of these factors, a unified standard can be established in this field, enabling rigorous comparison across different materials and further, more effective development of future solar thermal systems.

Author contributions

Y. W. conceived and drafted the manuscript. G. C., M. C., and D. M. supervised the review and revised the manuscript. All authors approved the final version.

Conflicts of interest

There are no conflicts to declare.

Data availability

No primary research results, software or code have been included, and no new data were generated or analysed as part of this review.

Acknowledgements

The authors acknowledge the financial support from the Natural Sciences and Engineering Research Council of Canada (NSERC) and Fonds de recherche du Quebec-Nature et technologies (FRQNT). D. M. is also grateful to the Canada Research Chairs Program.

References

1 C. He, Z. Liu, J. Wu, X. Pan, Z. Fang, J. Li and B. A. Bryan, *Nat. Commun.*, 2021, **12**, 4667.
2 A. M. Saleque, N. Nowshin, M. N. A. S. Ivan, S. Ahmed and Y. H. Tsang, *Sol. RRL*, 2022, **6**, 2100986.
3 M. Sadrzadeh and T. Mohammadi, *Desalination*, 2008, **221**, 440–447.
4 C. Fritzmann, J. Löwenberg, T. Wintgens and T. Melin, *Desalination*, 2007, **216**, 1–76.
5 S. Miller, H. Shemer and R. Semiat, *Desalination*, 2015, **366**, 2–8.
6 G. Liu, J. Shen, Q. Liu, G. Liu, J. Xiong, J. Yang and W. Jin, *J. Membr. Sci.*, 2018, **548**, 548–558.
7 P. Tao, G. Ni, C. Song, W. Shang, J. Wu, J. Zhu, G. Chen and T. Deng, *Nat. Energy*, 2018, **3**, 1031–1041.
8 K. Mao, Y. Zhang and S. C. Tan, *Nat. Water*, 2025, **3**, 144–156.
9 J. Sun, S. Zhao, X. Wang, W. Kong, W. Li, S. Wang, S. Liu and S. Nie, *Mater. Today*, 2024, **80**, 619–647.
10 M. Gao, L. Zhu, C. K. Peh and G. W. Ho, *Energy Environ. Sci.*, 2019, **12**, 841–864.
11 T. Ding, Y. Zhou, W. L. Ong and G. W. Ho, *Mater. Today*, 2021, **42**, 178–191.
12 L. Zhao, Z. Liu, D. Chen, F. Liu, Z. Yang, X. Li, H. Yu, H. Liu and W. Zhou, *Nano-Micro Lett.*, 2021, **13**, 49.
13 F. Zhao, Y. Guo, X. Zhou, W. Shi and G. Yu, *Nat. Rev. Mater.*, 2020, **5**, 388–401.
14 Q. Chen, Z. Pei, Y. Xu, Z. Li, Y. Yang, Y. Wei and Y. Ji, *Chem. Sci.*, 2018, **9**, 623–628.
15 K. Li, M. Gao, Z. Li, H. Yang, L. Jing, X. Tian, Y. Li, S. Li, H. Li and Q. Wang, *Nano Energy*, 2020, **74**, 104875.
16 F. L. Meng, M. Gao, T. Ding, G. Yilmaz, W. L. Ong and G. W. Ho, *Adv. Funct. Mater.*, 2020, **30**, 2002867.
17 M. Q. Yang, C. F. Tan, W. Lu, K. Zeng and G. W. Ho, *Adv. Funct. Mater.*, 2020, **30**, 2004460.
18 J. A. Schuller, E. S. Barnard, W. Cai, Y. C. Jun, J. S. White and M. L. Brongersma, *Nat. Mater.*, 2010, **9**, 193–204.
19 Z. Deng, J. Zhou, L. Miao, C. Liu, Y. Peng, L. Sun and S. Tanemura, *J. Mater. Chem. A*, 2017, **5**, 7691–7709.
20 J. Liang, H. Liu, J. Yu, L. Zhou and J. Zhu, *Nanophotonics*, 2019, **8**, 771–786.
21 J. Chen, Z. Ye, F. Yang and Y. Yin, *Small Sci.*, 2021, **1**, 2000055.
22 M. L. Brongersma, N. J. Halas and P. Nordlander, *Nat. Nanotechnol.*, 2015, **10**, 25–34.
23 Y. Wang, Y. Wang, I. Aravind, Z. Cai, L. Shen, B. Zhang, B. Wang, J. Chen, B. Zhao and H. Shi, *J. Am. Chem. Soc.*, 2022, **144**, 3517–3526.
24 M. Rycenga, C. M. Cobley, J. Zeng, W. Li, C. H. Moran, Q. Zhang, D. Qin and Y. Xia, *Chem. Rev.*, 2011, **111**, 3669–3712.
25 A. Agrawal, S. H. Cho, O. Zandi, S. Ghosh, R. W. Johns and D. J. Milliron, *Chem. Rev.*, 2018, **118**, 3121–3207.
26 J. T. Lee, S. Hati, M. M. Fahey, J. M. Zaleski and R. Sardar, *Chem. Mater.*, 2022, **34**, 3053–3066.
27 M. P. Wells, R. Bower, R. Kilmurray, B. Zou, A. P. Mihai, G. Gobalakrichenane, N. M. Alford, R. F. Oulton, L. F. Cohen and S. A. Maier, *Opt. Express*, 2018, **26**, 15726–15744.
28 U. Guler, J. C. Ndukaife, G. V. Naik, A. A. Nnanna, A. V. Kildishev, V. M. Shalaev and A. Boltasseva, *Nano Lett.*, 2013, **13**, 6078–6083.
29 G. Xie, C. Han, F. Song, Y. Zhu, X. Wang, J. Wang, Z. Wu, X. Xie and N. Zhang, *Nanoscale*, 2022, **14**, 18010–18021.
30 M. Huang, X. Wang, G. Xing, C. Meng, Y. Li, X. Li, L. Fan, Y. Wan and S. Yang, *J. Phys. Chem. Lett.*, 2021, **12**, 7988–7996.
31 X. Liu and M. T. Swihart, *Chem. Soc. Rev.*, 2014, **43**, 3908–3920.
32 L. M. Liz-Marzán, *Langmuir*, 2006, **22**, 32–41.
33 K. L. Kelly, E. Coronado, L. L. Zhao and G. C. Schatz, *J. Phys. Chem. B*, 2003, **107**, 668–677.
34 Y. Cao, R. Zheng, X. Ji, H. Liu, R. Xie and W. Yang, *Langmuir*, 2014, **30**, 3876–3882.

35 W. Haiss, N. T. K. Thanh, J. Aveyard and D. G. Fernig, *Anal. Chem.*, 2007, **79**, 4215–4221.
36 Y. Wang, Q. Zhang, Y. Wang, L. V. Besteiro, Y. Liu, H. Tan, Z. M. Wang, A. O. Govorov, J. Z. Zhang, J. K. Cooper, J. Zhao, G. Chen, M. Chaker and D. Ma, *Chem. Mater.*, 2021, **33**, 695–705.
37 Z. Fang, Y.-R. Zhen, O. Neumann, A. Polman, F. J. García de Abajo, P. Nordlander and N. J. Halas, *Nano Lett.*, 2013, **13**, 1736–1742.
38 Y. A. Attia, D. Buceta, F. G. Requejo, L. J. Giovanetti and M. A. López-Quintela, *Nanoscale*, 2015, **7**, 11273–11279.
39 S. Patskovsky, E. Bergeron, D. Rioux, M. Simard and M. Meunier, *Analyst*, 2014, **139**, 5247–5253.
40 X. Huang, I. H. El-Sayed, W. Qian and M. A. El-Sayed, *J. Am. Chem. Soc.*, 2006, **128**, 2115–2120.
41 W. Zhang, Q. Li and M. Qiu, *Opt. Express*, 2013, **21**, 172–181.
42 Y. Shen, J. Zhou, T. Liu, Y. Tao, R. Jiang, M. Liu, G. Xiao, J. Zhu, Z.-K. Zhou, X. Wang, C. Jin and J. Wang, *Nat. Commun.*, 2013, **4**, 2381.
43 A. Alvarez Barragan, N. V. Ilawe, L. Zhong, B. M. Wong and L. Mangolini, *J. Phys. Chem. C*, 2017, **121**, 2316–2322.
44 M. R. Kim, H. A. Hafez, X. Chai, L. V. Besteiro, L. Tan, T. Ozaki, A. O. Govorov, R. Izquierdo and D. Ma, *Nanoscale*, 2016, **8**, 12946–12957.
45 V. Amendola and M. Meneghetti, *Phys. Chem. Chem. Phys.*, 2009, **11**, 3805–3821.
46 S. Link, C. Burda, B. Nikoobakht and M. A. El-Sayed, *J. Phys. Chem. B*, 2000, **104**, 6152–6163.
47 A. Lalisse, G. Tessier, J. Plain and G. Baffou, *J. Phys. Chem. C*, 2015, **119**, 25518–25528.
48 A. O. Govorov and H. H. Richardson, *Nano Today*, 2007, **2**, 30–38.
49 G. Baffou, R. Quidant and C. Girard, *Appl. Phys. Lett.*, 2009, **94**, 153109.
50 D. K. Roper, W. Ahn and M. Hoepfner, *J. Phys. Chem. C*, 2007, **111**, 3636–3641.
51 V. P. Pattani and J. W. Tunnell, *Lasers Surg. Med.*, 2012, **44**, 675–684.
52 Y. Wang, X. Liu, Q. Zhang, C. Wang, S. Huang, Y. Liu, T. Yu, R. Yang, G. Chen, M. Chaker and D. Ma, *Adv. Funct. Mater.*, 2023, **33**, 2212301.
53 C. M. Hessel, V. P. Pattani, M. Rasch, M. G. Panthani, B. Koo, J. W. Tunnell and B. A. Korgel, *Nano Lett.*, 2011, **11**, 2560–2566.
54 Q. Tian, F. Jiang, R. Zou, Q. Liu, Z. Chen, M. Zhu, S. Yang, J. Wang, J. Wang and J. Hu, *ACS Nano*, 2011, **5**, 9761–9771.
55 J. Ge, Q. Jia, W. Liu, M. Lan, B. Zhou, L. Guo, H. Zhou, H. Zhang, Y. Wang, Y. Gu, X. Meng and P. Wang, *Adv. Healthcare Mater.*, 2016, **5**, 665–675.
56 D. Ding, W. Guo, C. Guo, J. Sun, N. Zheng, F. Wang, M. Yan and S. Liu, *Nanoscale*, 2017, **9**, 2020–2029.
57 J. He, L. Ai, X. Liu, H. Huang, Y. Li, M. Zhang, Q. Zhao, X. Wang, W. Chen and H. Gu, *J. Mater. Chem. B*, 2018, **6**, 1035–1043.
58 Q. Wang, H. Wang, Y. Yang, L. Jin, Y. Liu, Y. Wang, X. Yan, J. Xu, R. Gao, P. Lei, J. Zhu, Y. Wang, S. Song and H. Zhang, *Adv. Mater.*, 2019, **31**, 1904836.
59 H. Ghasemi, G. Ni, A. M. Marconnet, J. Loomis, S. Yerci, N. Miljkovic and G. Chen, *Nat. Commun.*, 2014, **5**, 4449.
60 O. Neumann, A. S. Urban, J. Day, S. Lal, P. Nordlander and N. J. Halas, *ACS Nano*, 2013, **7**, 42–49.
61 K. Bae, G. Kang, S. K. Cho, W. Park, K. Kim and W. J. Padilla, *Nat. Commun.*, 2015, **6**, 10103.
62 S. Cao, A. Thomas and C. Li, *Angew. Chem., Int. Ed.*, 2022, **62**, e202214391.
63 Y. Ito, Y. Tanabe, J. Han, T. Fujita, K. Tanigaki and M. Chen, *Adv. Mater.*, 2015, **27**, 4302–4307.
64 M. Zhu, Y. Li, F. Chen, X. Zhu, J. Dai, Y. Li, Z. Yang, X. Yan, J. Song, Y. Wang, E. Hitz, W. Luo, M. Lu, B. Yang and L. Hu, *Adv. Energy Mater.*, 2018, **8**, 1701028.
65 L. Ren, X. Yi, Z. Yang, D. Wang, L. Liu and J. Ye, *Nano Lett.*, 2021, **21**, 1709–1715.
66 L. Zhou, Y. Tan, J. Wang, W. Xu, Y. Yuan, W. Cai, S. Zhu and J. Zhu, *Nat. Photonics*, 2016, **10**, 393–398.
67 F. Yang, J. Chen, Z. Ye, D. Ding, N. V. Myung and Y. Yin, *Adv. Funct. Mater.*, 2021, **31**, 2006294.
68 J. Xu, F. Xu, M. Qian, Z. Li, P. Sun, Z. Hong and F. Huang, *Nano Energy*, 2018, **53**, 425–431.
69 L. Zhang, J. Xing, X. Wen, J. Chai, S. Wang and Q. Xiong, *Nanoscale*, 2017, **9**, 12843–12849.
70 C. Tian, C. Li, D. Chen, Y. Li, L. Xing, X. Tian, Y. Cao, W. Huang, Z. Liu and Y. Shen, *J. Mater. Chem. A*, 2021, **9**, 15462–15471.
71 F. Meng, Z. Ding, Z. Chen, K. Wang, X. Liu, J. Li, T. Lu, X. Xu and L. Pan, *J. Mater. Chem. A*, 2022, **10**, 9575–9581.
72 Z. Wang, Y. Liu, P. Tao, Q. Shen, N. Yi, F. Zhang, Q. Liu, C. Song, D. Zhang, W. Shang and T. Deng, *Small*, 2014, **10**, 3234–3239.
73 H. Hu, Z. Wang, Q. Ye, J. He, X. Nie, G. He, C. Song, W. Shang, J. Wu, P. Tao and T. Deng, *ACS Appl. Mater. Interfaces*, 2016, **8**, 20483–20490.
74 J. Chen, J. Feng, Z. Li, P. Xu, X. Wang, W. Yin, M. Wang, X. Ge and Y. Yin, *Nano Lett.*, 2018, **19**, 400–407.
75 Y. Zhang, Y. Wang, B. Yu, K. Yin and Z. Zhang, *Adv. Mater.*, 2022, **34**, 2200108.
76 L. Zhou, Y. Tan, D. Ji, B. Zhu, P. Zhang, J. Xu, Q. Gan, Z. Yu and J. Zhu, *Sci. Adv.*, 2016, **2**, e1501227.
77 Y. Liu, Z. Liu, Q. Huang, X. Liang, X. Zhou, H. Fu, Q. Wu, J. Zhang and W. Xie, *J. Mater. Chem. A*, 2019, **7**, 2581–2588.
78 M. Chen, Y. Wu, W. Song, Y. Mo, X. Lin, Q. He and B. Guo, *Nanoscale*, 2018, **10**, 6186–6193.
79 L. Zhou, S. Zhuang, C. He, Y. Tan, Z. Wang and J. Zhu, *Nano Energy*, 2017, **32**, 195–200.
80 M. Wang, P. Wang, J. Zhang, C. Li and Y. Jin, *ChemSusChem*, 2019, **12**, 467–472.
81 Y. Liu, S. Yu, R. Feng, A. Bernard, Y. Liu, Y. Zhang, H. Duan, W. Shang, P. Tao, C. Song and T. Deng, *Adv. Mater.*, 2015, **27**, 2768–2774.
82 J. Qiu, M. Xie, T. Wu, D. Qin and Y. Xia, *Chem. Sci.*, 2020, **11**, 12955–12973.
83 D. Guo and X. Yang, *Sci. China Mater.*, 2019, **62**, 711–718.
84 E. Traver, R. A. Karaballi, Y. E. Monfared, H. Daurie, G. A. Gagnon and M. Dasog, *ACS Appl. Nano Mater.*, 2020, **3**, 2787–2794.

85 M. Kaur, S. Ishii, S. L. Shinde and T. Nagao, *ACS Sustainable Chem. Eng.*, 2017, **5**, 8523–8528.
86 M. Kaur, S. Ishii, S. L. Shinde and T. Nagao, *Adv. Sustainable Syst.*, 2019, **3**, 1800112.
87 M. U. Farid, J. A. Kharraz, P. Wang and A. K. An, *J. Cleaner Prod.*, 2020, **271**, 122684.
88 L. Mascaretti, A. Schirato, R. Zbořil, Š. Kment, P. Schmuki, A. Alabastri and A. Naldoni, *Nano Energy*, 2021, **83**, 105828.
89 Y. Bian, K. Tang, Z. Xu, J. Ma, Y. Shen, L. Hao, X. Chen, K. Nie, J. Li, T. Ma, S. Zhu, J. Ye, X. Xiong, Y. Yang, R. Zhang, Y. Zheng and S. Gu, *J. Mater. Res.*, 2018, **33**, 3857–3869.
90 C. Zhang, C. Yan, Z. Xue, W. Yu, Y. Xie and T. Wang, *Small*, 2016, **12**, 5320–5328.
91 N. Li, D. Yin, L. Xu, H. Zhao, Z. Liu and Y. Du, *Mater. Chem. Front.*, 2019, **3**, 394–398.
92 F. Tao, Y. Zhang, K. Yin, S. Cao, X. Chang, Y. Lei, D. Wang, R. Fan, L. Dong, Y. Yin and X. Chen, *Sustainable Energy Fuels*, 2018, **2**, 2762–2769.
93 M. Shang, N. Li, S. Zhang, T. Zhao, C. Zhang, C. Liu, H. Li and Z. Wang, *ACS Appl. Energy Mater.*, 2018, **1**, 56–61.
94 F. Tao, Y. Zhang, S. Cao, K. Yin, X. Chang, Y. Lei, R. Fan, L. Dong, Y. Yin and X. Chen, *Mater. Today Energy*, 2018, **9**, 285–294.
95 X. Li, D. Wang, Y. Zhang, L. Liu and W. Wang, *Nano Res.*, 2020, **13**, 3025–3032.
96 Z. Li, M. Zheng, N. Wei, Y. Lin, W. Chu, R. Xu, H. Wang, J. Tian and H. Cui, *Sol. Energy Mater. Sol. Cells*, 2020, **205**, 110254.
97 Q. Lu, Y. Yang, J. Feng and X. Wang, *Sol. RRL*, 2019, **3**, 1800277.
98 S. K. Balu, R. Xing and S. Liu, *Sustainable Mater. Technol.*, 2024, e00941.
99 O. Neumann, C. Feronti, A. D. Neumann, A. Dong, K. Schell, B. Lu, E. Kim, M. Quinn, S. Thompson, N. Grady, P. Nordlander, M. Oden and N. J. Halas, *Proc. Natl. Acad. Sci. U. S. A.*, 2013, **110**, 11677–11681.
100 D. Zhao, H. Duan, S. Yu, Y. Zhang, J. He, X. Quan, P. Tao, W. Shang, J. Wu, C. Song and T. Deng, *Sci. Rep.*, 2015, **5**, 17276.
101 L. Tian, J. Luan, K.-K. Liu, Q. Jiang, S. Tadepalli, M. K. Gupta, R. R. Naik and S. Singamaneni, *Nano Lett.*, 2016, **16**, 609–616.
102 G. Zhu, G. Jing, G. Xu, Q. Li, R. Huang, F. Li, H. Li, D. Wang, W. Chen and B. Z. Tang, *Nano Res.*, 2022, **15**, 6705–6712.
103 B. Yu, Y. Wang, Y. Zhang and Z. Zhang, *Nano Res.*, 2022, **16**, 5610–5618.
104 Y. Xu, J. Ma, Y. Han, H. Xu, Y. Wang, D. Qi and W. Wang, *Chem. Eng. J.*, 2020, **384**, 123379.
105 Z. Sun, J. Wang, Q. Wu, Z. Wang, Z. Wang, J. Sun and C.-J. Liu, *Adv. Funct. Mater.*, 2019, **29**, 1901312.
106 Y. Chen, J. Fang, T. Ling, M. Xia, P. Xu, Y. Cao, D. Wei and J. Gao, *Desalination*, 2022, **541**, 116003.
107 S. Chen, Z. Sun, W. Xiang, C. Shen, Z. Wang, X. Jia, J. Sun and C.-J. Liu, *Nano Energy*, 2020, **76**, 104998.
108 B. Sharma and M. K. Rabinal, *J. Alloys Compd.*, 2017, **690**, 57–62.
109 Z. Wang, Y. Yan, X. Shen, C. Jin, Q. Sun and H. Li, *J. Mater. Chem. A*, 2019, **7**, 20706–20712.
110 J. Zhou, Y. Gu, P. Liu, P. Wang, L. Miao, J. Liu, A. Wei, X. Mu, J. L. Li and J. Zhu, *Adv. Funct. Mater.*, 2019, **29**, 1903255.
111 M. Gao, C. K. Peh, L. Zhu, G. Yilmaz and G. W. Ho, *Adv. Energy Mater.*, 2020, **10**, 2000925.
112 S. Tyagi, R. K. Kashyap, A. Dhankhar and P. P. Pillai, *Chem. Sci.*, 2024, **15**, 16997–17006.
113 P. Fan, H. Wu, M. Zhong, H. Zhang, B. Bai and G. Jin, *Nanoscale*, 2016, **8**, 14617–14624.
114 N. Li, D.-J. Yang, Y. Shao, Y. Liu, J. Tang, L. Yang, T. Sun, W. Zhou, H. Liu and G. Xue, *ACS Appl. Mater. Interfaces*, 2021, **13**, 4305–4315.
115 L. Li, J. Wang, B. Jiao, X. Zuo, Z. Wang, X. He, H. Dong, X. Hou and Z. Wu, *Org. Electron.*, 2023, **114**, 106727.
116 Y. Huang, Y. Morishita, K. Uetani, M. Nogi and H. Koga, *Nanoscale Adv.*, 2020, **2**, 2339–2346.
117 M. Gao, C. K. Peh, H. T. Phan, L. Zhu and G. W. Ho, *Adv. Energy Mater.*, 2018, **8**, 1800711.
118 P. Sun, J. Liu, W. Zhang and D. Zhang, *Energy Technol.*, 2024, 2301393.
119 X. Wang, K. Liu, Z. Wang, L. Heng and L. Jiang, *J. Mater. Chem. A*, 2022, **10**, 3436–3442.
120 P. Sun, W. Wang, W. Zhang, S. Zhang, J. Gu, L. Yang, D. Pantelić, B. Jelenković and D. Zhang, *ACS Appl. Mater. Interfaces*, 2020, **12**, 34837–34847.
121 Y. Chen, Z. Mao, J. Yin, J. Shen, W. Ou and J. Lu, *Sep. Purif. Technol.*, 2023, **325**, 124637.
122 H. Wang, R. Zhang, D. Yuan, S. Xu and L. Wang, *Adv. Funct. Mater.*, 2020, **30**, 2003995.
123 Z. Zheng, H. Li, X. Zhang, H. Jiang, X. Geng, S. Li, H. Tu, X. Cheng, P. Yang and Y. Wan, *Nano Energy*, 2020, **68**, 104298.
124 J. Zhou, Y. Gu, Z. Deng, L. Miao, H. Su, P. Wang and J. Shi, *Sustainable Mater. Technol.*, 2019, **19**, e00090.
125 X. Wang, Y. He and X. Liu, *Energy Convers. Manage.*, 2018, **173**, 158–166.
126 Z. Sun, F. Huang, Y. Cai, W. Liang, S. Fan, C. Tu, Y. Liu and C. Yan, *Chem. Eng. J.*, 2024, 152309.
127 J. Xu, Y. Chen, M. Cao, C. Wang and P. Guo, *J. Mater. Res.*, 2022, **37**, 1475–1485.
128 Z. Huang, S. Li, X. Cui, Y. Wan, Y. Xiao, S. Tian, H. Wang, X. Li, Q. Zhao and C.-S. Lee, *J. Mater. Chem. A*, 2020, **8**, 10742–10746.
129 A. Roy, M. Z. Tariq, M. La, D. Choi and S. J. Park, *Desalination*, 2023, **563**, 116732.
130 L. Ren, W. Zhou, L. Wang, K. Lin, Y. Xu, J. Wu, Y. Xie and H. Fu, *Sci. Bull.*, 2023, **68**, 2760–2768.
131 C. Gao, Y. Chen, Q. Wang, B. Zhou, J. Li, J. Mao and J. Guo, *Sep. Purif. Technol.*, 2023, **323**, 124477.
132 C. Xiao, W. Liang, Q.-M. Hasi, L. Chen, J. He, F. Liu, C. Wang, H. Sun, Z. Zhu and A. Li, *Mater. Today Energy*, 2020, **16**, 100417.
133 P. Qiao, J. Wu, H. Li, Y. Xu, L. Ren, K. Lin and W. Zhou, *ACS Appl. Mater. Interfaces*, 2019, **11**, 7066–7073.

134 S. Luo, Z. Liu, X. Yin, Z. Lin, S. Zhang, J. Chen and M. Guo, *Small*, 2024, 2309087.
135 L. Li, K. Zeng, Z. He, J. Xue, X. Liu, A. Liu, L. Gao and T. Ma, *Energy Technol.*, 2023, **11**, 2201284.
136 Y. A. Younes, D. A. Kospa, R. S. Salama, A. I. Ahmed and A. A. Ibrahim, *Desalination*, 2023, **550**, 116377.
137 S.-J. Wang, D. Su, H.-L. Zhou, X. Yan, X.-Y. Zhang and T. Zhang, *Compos. Commun.*, 2023, **38**, 101516.
138 Y. Liu, J. Xiong, A. Li, R. Wang, L. Wang and X. Qin, *Text. Res. J.*, 2021, **91**, 2624–2634.
139 Y. Shi, C. Zhang, Y. Wang, Y. Cui, Q. Wang, G. Liu, S. Gao and Y. Yuan, *Desalination*, 2021, **507**, 115038.
140 X. Cao, W. Dong, J. Yan, G. Meng, Z. Liu and J. Wu, *Sol. Energy*, 2023, **255**, 26–35.
141 J. Xu, R. Cui, C. Zhou and S. Yang, *Desalination*, 2024, **573**, 117204.
142 R. Song, N. Zhang, P. Wang, H. Ding and S. Li, *Sep. Purif. Technol.*, 2024, **342**, 126964.
143 T. S. Shridharan, A. Sivanantham, R. Tan, S. Y. Hong, D. H. Kim and I. S. Cho, *Desalination*, 2023, **561**, 116700.
144 S. Higashi, T. Matsui and A. Beniya, *ACS Appl. Mater. Interfaces*, 2022, **14**, 40214–40222.
145 K. Wang, D. Y. Wang, M. Z. Wang, X. X. Dan, L. M. Che, H. H. Xu, H. Zhou, H. Liu, L. Singh and X. E. Wu, *Sol. Energy Mater. Sol. Cells*, 2020, **204**, 110203.
146 C. Liu, C. Cai, F. Ma, X. Zhao and H. Ahmad, *J. Colloid Interface Sci.*, 2020, **560**, 103–110.
147 D. A. Kospa, A. I. Ahmed, S. E. Samra and A. A. Ibrahim, *RSC Adv.*, 2021, **11**, 15184–15194.
148 L. Zhao, C. Du, C. Zhou, S. Sun, Y. Jia, J. Yuan, G. Song, X. Zhou, Q. Zhao and S. Yang, *ACS Sustainable Chem. Eng.*, 2020, **8**, 4362–4370.
149 H. Li, Y. He, Z. Liu, B. Jiang and Y. Huang, *Energy*, 2017, **139**, 210–219.
150 S. Chen, C. G. Yoo, D. Yang, X. Qiu and D. Zheng, *Desalination*, 2023, **556**, 116572.
151 D. Wu, C. Zhao, Y. Xu, X. Zhang, L. Yang, Y. Zhang, Z. Gao and Y.-Y. Song, *ACS Appl. Nano Mater.*, 2020, **3**, 10895–10904.
152 J. Fang, Q. Liu, W. Zhang, J. Gu, Y. Su, H. Su, C. Guo and D. Zhang, *J. Mater. Chem. A*, 2017, **5**, 17817–17821.
153 J. Yang, Y. Chen, X. Jia, Y. Li, S. Wang and H. Song, *ACS Appl. Mater. Interfaces*, 2020, **12**, 47029–47037.
154 M. Simayee and A. Esfandiar, *Sol. Energy*, 2023, **265**, 112097.
155 Y. Tan, H. Jin, S. S. Mao and S. Shen, *Carbon Neutrality*, 2023, **2**, 11.
156 X. Wu, C. Li, Z. Zhang, Y. Cao, J. Wang, X. Tian, Z. Liu, Y. Shen, M. Zhang and W. Huang, *Carbon Energy*, 2024, **6**, e466.
157 M. Simayee, A. Iraji zad and A. Esfandiar, *Sci. Rep.*, 2023, **13**, 12762.
158 D. Xu, H. Zhong, M. G. Li, S. S. To and L. Lu, *Carbon*, 2023, **204**, 231–237.
159 X. Zhang, X. Wang, W. D. Wu, X. D. Chen and Z. Wu, *J. Mater. Chem. A*, 2019, **7**, 6963–6971.
160 J. Jiang, R. Yang, Z. Tao and S. Tu, *Desalination*, 2024, **569**, 117034.
161 W. Wang, X. Yan, J. Geng, N. Zhao, L. Liu, T. Vogel, Q. Guo, L. Ge, B. Luo and Y. Zhao, *ACS Nano*, 2021, **15**, 16376–16394.
162 P. Cheng, M. Klingenhof, H. Honig, L. Zhang, P. Strasser, P. Schaaf, D. Lei and D. Wang, *Adv. Mater.*, 2025, **37**, 2415655.
163 J. Jiang, Y. Xu, C. Tang, X. Wang, W. Wei and L. Ai, *Desalination*, 2023, **560**, 116680.
164 L. Ying, Z. Yuan, J. Ding, W. Wang, S. Liu and J. Lu, *Chem. Eng. J.*, 2024, **487**, 150593.
165 R. Song, N. Zhang, P. Wang, H. Ding, J. Wang and S. Li, *Appl. Surf. Sci.*, 2023, **616**, 156448.
166 L. Cui, P. Wang, H. Che, X. Gao, J. Chen, B. Liu and Y. Ao, *Appl. Catal., B*, 2023, **330**, 122556.
167 A. Mowafy, A. A. Ibrahim, A. Gebreil, R. M. Eltabey, A. I. Ahmed and M. S. Adly, *Desalination*, 2024, **574**, 117288.
168 H. D. Kiriarachchi, F. S. Awad, A. A. Hassan, J. A. Bobb, A. Lin and M. S. El-Shall, *Nanoscale*, 2018, **10**, 18531–18539.
169 B.-J. Ku, D. H. Kim, A. S. Yasin, A. Mnoyan, M.-J. Kim, Y. J. Kim, H. Ra and K. Lee, *J. Colloid Interface Sci.*, 2023, **634**, 543–552.
170 F. Pini, R. Pilot, G. Ischia, S. Agnoli and V. Amendola, *ACS Appl. Mater. Interfaces*, 2022, **14**, 28924–28935.
171 A. G. Saad, A. Gebreil, D. A. Kospa, S. El-Hakam and A. A. Ibrahim, *Desalination*, 2022, **535**, 115824.
172 W. Song, H. Wang, Z. Zhang, Y. Cao, M. Zhang, P. Zhang, Y. Zhang, Z. Liu, Y. Shen and W. Huang, *J. Colloid Interface Sci.*, 2023, **650**, 1044–1051.
173 F. S. Awad, H. D. Kiriarachchi, K. M. AbouZeid, Ü. Özgur and M. S. El-Shall, *ACS Appl. Energy Mater.*, 2018, **1**, 976–985.
174 H. Li, S. Gao, H. Ding, Y. Tao, S. Ma, G. Wang and B. Wang, *ACS Appl. Energy Mater.*, 2023, **6**, 5989–5996.
175 Y. Tao, Y. Mi, S. Gao, G. Wang, J. Bai, S. Ma and B. Wang, *Chem. Eng. J.*, 2023, **477**, 147276.
176 D. A. Kospa, A. Gebreil, S. A. El-Hakam, A. I. Ahmed and A. A. Ibrahim, *J. Mater. Res. Technol.*, 2023, **23**, 2924–2939.
177 U. Guler, V. M. Shalaev and A. Boltasseva, *Mater. Today*, 2015, **18**, 227–237.
178 M. J. Margeson and M. Dasog, *Environ. Sci.: Water Res. Technol.*, 2020, **6**, 3169–3177.
179 L. Wang, J. Shang, G. Yang, Y. Ma, L. Kou, D. Liu, H. Yin, D. Hegh, J. Razal and W. Lei, *Small*, 2022, **18**, 2201770.
180 M. Kumar, N. Umezawa, S. Ishii and T. Nagao, *ACS Photonics*, 2016, **3**, 43–50.
181 R. A. Karaballi, Y. Esfahani Monfared and M. Dasog, *Langmuir*, 2020, **36**, 5058–5064.
182 Y. Zhang, K. Li, L. Liu, K. Wang, J. Xiang, D. Hou and J. Wang, *Chemosphere*, 2020, **256**, 127053.
183 P. Ren and X. Yang, *Sol. RRL*, 2018, **2**, 1700233.
184 I. V. Zelepukin, A. A. Popov, V. O. Shipunova, G. V. Tikhonowski, A. B. Mirkasymov, E. A. Popova-Kuznetsova, S. M. Klimentov, A. V. Kabashin and S. M. Deyev, *Mater. Sci. Eng., C*, 2021, **120**, 111717.

185 J. Li, L. Gao, J. Sun, Q. Zhang, J. Guo and D. Yan, *J. Am. Ceram. Soc.*, 2001, **84**, 3045–3047.
186 X. Bai, S. H. Lam, J. Hu, K. K. Chui, X.-M. Zhu, L. Shao, T. H. Chow and J. Wang, *ACS Appl. Mater. Interfaces*, 2023, **15**, 55856–55869.
187 M. U. Farid, J. A. Kharraz and A. K. An, *ACS Appl. Mater. Interfaces*, 2021, **13**, 3805–3815.
188 Y. Gao, X. Zhou, N. Fu, S. Su, B. Ma, Q. Ruan, D. Wu, N. Zhang, Z. Deng and R. Jiang, *Chem. Eng. J.*, 2023, **475**, 146078.
189 X. Shan, Z. Yin, Y. Jia, F. Liu, Y. Wang, J. Kong, X. Song, M. Zhang, Y. Li, H. Zhang, F. Meng, D. Ma, Q. Zhang, Y. Yin and Y. Cai, *Adv. Funct. Mater.*, 2025, e14279.
190 L. Ying, F. Liang, Z. Huang, J. Ding, W. Wang, S. Liu and J. Lu, *Chem. Eng. J.*, 2023, **474**, 145709.
191 C. Xue, Y. Shen, Q. Zhang, Q. Chang, N. Li, Y. Li, W. Zheng, S. Hu and J. Yang, *Nano Res.*, 2022, **16**, 5953–5963.
192 H. Cheng, W. Xia, Z. Zhao, W. Wang, K. Song, H. Li, C. Cheng and H. Hu, *J. Mater. Sci.*, 2022, **57**, 11725–11734.
193 C. Chen, H. Liu, H. Wang, Y. Zhao and M. Li, *Nano Energy*, 2021, **84**, 105868.
194 Q. Zhang, A. Mirzaei, Y. Wang, G. Song, C. Wang, L. V. Besteiro, A. O. Govorov, M. Chaker and D. Ma, *Appl. Catal., B*, 2022, **317**, 121792.
195 F. Tao, Y. Zhang, K. Yin, S. Cao, X. Chang, Y. Lei, D. S. Wang, R. Fan, L. Dong, Y. Yin and X. Chen, *ACS Appl. Mater. Interfaces*, 2018, **10**, 35154–35163.
196 Z. Xu, N. Rao, C.-Y. Tang and W.-C. Law, *Micromachines*, 2020, **11**, 867.
197 H. S. Kang, J. W. Zou, Y. Liu, L. Ma, J. R. Feng, Z. Y. Yu, X. B. Chen, S. J. Ding, L. Zhou and Q. Q. Wang, *Adv. Funct. Mater.*, 2023, **33**, 2303911.
198 S. Chhetri, A. T. Nguyen, S. Song, D. H. Park, T. Ma, N. Gaillard, S.-H. Yoon and W. Lee, *ACS Appl. Mater. Interfaces*, 2023, **15**, 54773–54785.
199 M. Shang, S. Xu, J. Li, H. Sun, J. Peng, S. Wang and M. Zhang, *Energy Technol.*, 2022, **10**, 2100805.
200 S.-L. Gong, Y. Tian, G.-P. Sheng and L.-J. Tian, *Nat. Commun.*, 2024, **15**, 4365.
201 I. Ibrahim, D. H. Seo, A. M. McDonagh, H. K. Shon and L. Tijing, *Desalination*, 2021, **500**, 114853.
202 D. Ding, W. Huang, C. Song, M. Yan, C. Guo and S. Liu, *Chem. Commun.*, 2017, **53**, 6744–6747.
203 X. Ming, A. Guo, G. Wang and X. Wang, *Sol. Energy Mater. Sol. Cells*, 2018, **185**, 333–341.
204 Z. Li, N. Wei, M. Zheng, A. Yao, R. Xu, X. Song, H. Wang, Q. Liu and H. Cui, *Powder Technol.*, 2020, **361**, 817–826.
205 T. Wang, S. Gao, G. Wang, H. Wang, J. Bai, S. Ma and B. Wang, *J. Colloid Interface Sci.*, 2021, **602**, 767–777.
206 T. F. Chala, C.-M. Wu, M.-H. Chou and Z.-L. Guo, *ACS Appl. Mater. Interfaces*, 2018, **10**, 28955–28962.
207 S. Huang, Y. Long, H. Yi, Z. Yang, L. Pang, Z. Jin, Q. Liao, L. Zhang, Y. Zhang, Y. Chen, H. Cui, J. Lu, X. Peng, H. Liang, S. Ruan and Y.-J. Zeng, *Appl. Surf. Sci.*, 2019, **491**, 328–334.
208 L. Gong, C. Li, N. Wei, J. Li, J. Shen, R. Xu, Q. Li, J. Tian and H. Cui, *Sep. Purif. Technol.*, 2021, **275**, 119139.
209 Y. Wang, W. He, R. Yang, D. Pohl, B. Rellinghaus, P. A. C. Neathway, Z. Kalantari Bolaghi, C. Wang, T. Yu, F. Yang, G. Chen, M. Chaker, A. Yurtsever, G. A. Botton, Y. Liu and D. Ma, *Nano Lett.*, 2024, **24**, 10987–10994.
210 Y. Chang, Z. Wang, Y.-E. Shi, X. Ma, L. Ma, Y. Zhang and J. Zhan, *J. Mater. Chem. A*, 2018, **6**, 10939–10946.
211 Z. Fang, S. Jiao, B. Wang, W. Yin and G. Pang, *Global Challenges*, 2019, **3**, 1800085.
212 L. Ren, X. Yang, X. Sun and Y. Yuan, *Nano Lett.*, 2023, **24**, 715–723.
213 B. Wang, T. Wang, S. Ma, J. Bai and H. Ma, *J. Colloid Interface Sci.*, 2024, **660**, 192–202.
214 J. Ren, Z. Liu, Q. Li, L. Chen, J. Gong, H. Wang, Y. Li, J. Qu and R. Niu, *ACS Appl. Mater. Interfaces*, 2024, **16**, 18855–18866.
215 R. Li, L. Zhang, L. Shi and P. Wang, *ACS Nano*, 2017, **11**, 3752–3759.
216 M. Naguib, M. Kurtoglu, V. Presser, J. Lu, J. Niu, M. Heon, L. Hultman, Y. Gogotsi and M. W. Barsoum, *Adv. Mater.*, 2011, **23**, 4248–4253.
217 X. Zhao, X.-J. Zha, L.-S. Tang, J.-H. Pu, K. Ke, R.-Y. Bao, Z.-Y. Liu, M.-B. Yang and W. Yang, *Nano Res.*, 2020, **13**, 255–264.
218 R. Ding, J. Xiong, Q. Yan, Z. Chen, Z. Liu, X. Zhao, Q. Peng and X. He, *Mater. Horiz.*, 2023, **10**, 2262–2270.
219 Y. Lu, D. Fan, Y. Wang, H. Xu, C. Lu and X. Yang, *ACS Nano*, 2021, **15**, 10366–10376.
220 Z. Y. Wang, Y. J. Zhu, Y. Q. Chen, H. P. Yu and Z. C. Xiong, *Small*, 2023, **19**, 2206917.
221 W. Zhou, N. Arshad, B. Xiao, X. Xiong, F. Yu, S. He, M. S. Irshad, X. Wang and L. Lin, *Next Nanotechnol.*, 2024, **5**, 100040.
222 D. Jiang, C. J. O. Bacal, K. A. S. Usman, J. Zhang, S. Qin, D. Hegh, W. Lei, J. Liu and J. M. Razal, *Adv. Mater. Technol.*, 2023, **8**, 2201611.
223 J. Yan, H. Kong, Y. Li, Q. Wang, X. Liu and Y. Wang, *Nano Lett.*, 2024, **24**, 3515–3524.
224 F. Su, Z. He, J. Xie, J. Zhang, W. Zhang, Y. Xin, A. Zhang, D. Yao and Y. Zheng, *J. Mater. Chem. A*, 2023, **11**, 20651–20664.
225 J. Wu, D. Liu, Y. Sun, B. Wei, K. Dai, Y. Sun, F. Zhang, C. Li, J. Xue and Z. Zhu, *Carbon*, 2024, 118976.
226 X.-J. Zha, X. Zhao, J.-H. Pu, L.-S. Tang, K. Ke, R.-Y. Bao, L. Bai, Z.-Y. Liu, M.-B. Yang and W. Yang, *ACS Appl. Mater. Interfaces*, 2019, **11**, 36589–36597.
227 Y. Wang, J. Nie, Z. He, Y. Zhi, X. Ma and P. Zhong, *ACS Appl. Mater. Interfaces*, 2022, **14**, 5876–5886.
228 Z. Zheng, W. Li, H. Liu and X. Wang, *ACS Appl. Mater. Interfaces*, 2022, **14**, 50966–50981.
229 Y. Jin, K. Wang, S. Li and J. Liu, *J. Colloid Interface Sci.*, 2022, **614**, 345–354.
230 Y. Bai, Y. Gu, J. Chen and Y. Yue, *J. Environ. Chem. Eng.*, 2024, 112282.
231 X. Ming, A. Guo, Q. Zhang, Z. Guo, F. Yu, B. Hou, Y. Wang, K. P. Homewood and X. Wang, *Carbon*, 2020, **167**, 285–295.
232 W. Li, X. Li, W. Chang, J. Wu, P. Liu, J. Wang, X. Yao and Z.-Z. Yu, *Nano Res.*, 2020, **13**, 3048–3056.

233 K. Li, T. H. Chang, Z. Li, H. Yang, F. Fu, T. Li, J. S. Ho and P. Y. Chen, *Adv. Energy Mater.*, 2019, **9**, 1901687.
234 Z. Yang, N. Wei, N. Xue, R. Xu, E. Yang, F. Wang, H. Zhu and H. Cui, *J. Colloid Interface Sci.*, 2024, **656**, 189–199.
235 A. M. Saleque, S. Ma, A. K. Thakur, R. Saidur, T. K. Han, M. I. Hossain, W. Qarony, Y. Ma, R. Sathyamurthy and Y. H. Tsang, *Desalination*, 2023, **554**, 116488.
236 Z. Wang, K. Yu, S. Gong, H. Mao, R. Huang and Z. Zhu, *ACS Appl. Mater. Interfaces*, 2021, **13**, 16246–16258.
237 Y. Wang, Y. Li, Q. Huang, W. Qi, R. Zan, M. Gan, Z. Rao and L. Fei, *Desalination*, 2023, **566**, 116910.
238 C. Liu and P. Wu, *RSC Adv.*, 2024, **14**, 10370–10377.
239 B. Zhang, Q. Gu, C. Wang, Q. Gao, J. Guo, P. W. Wong, C. T. Liu and A. K. An, *ACS Appl. Mater. Interfaces*, 2021, **13**, 3762–3770.
240 H. Li, L. Li, L. Xiong, B. Wang, G. Wang, S. Ma and X. Han, *ACS Appl. Nano Mater.*, 2021, **4**, 14274–14284.
241 C. Cai, Y. Wang, Z. Wei and Y. Fu, *Sol. RRL*, 2021, **5**, 2100593.
242 S. Chen, D. Zheng, Q. Cen, C. G. Yoo, L. Zhong, D. Yang and X. Qiu, *Small*, 2024, 2400603.
243 J. Chang, B. Pang, H. Zhang, K. Pang, M. Zhang and J. Yuan, *Adv. Fiber Mater.*, 2024, **6**, 252–263.
244 M. Singh, S. Qin, K. A. Usman, L. Wang, D. Jiang, G. Yang, D. Liu, Y. Ma and W. Lei, *Adv. Energy Sustainability Res.*, 2024, **5**, 2300126.
245 H. Gao, N. Bing, Z. Bao, H. Xie and W. Yu, *Chem. Eng. J.*, 2023, **454**, 140362.
246 Z. Liu, F. Wu, T. Lv, Y. Qu, Z. Zhang, C. Yu, C. Zhao and G. Xing, *Desalination*, 2024, **573**, 117207.
247 P.-L. Wang, W. Zhang, Q. Yuan, T. Mai, M.-Y. Qi and M.-G. Ma, *J. Colloid Interface Sci.*, 2023, **645**, 306–318.
248 D. Fan, Y. Lu, H. Zhang, H. Xu, C. Lu, Y. Tang and X. Yang, *Appl. Catal., B*, 2021, **295**, 120285.
249 N. Arshad, M. S. Irshad, M. S. Asghar, M. Alomar, J. Tao, M. Y. Shah, X. Wang, J. Guo, S. Wageh and O. A. Al-Hartomy, *Global Challenges*, 2023, **7**, 2300091.
250 C. Niu, L. Yang, H. Sun, Z. Zhu, W. Liang, J. Li and A. Li, *Chem. Eng. J.*, 2023, **476**, 146522.
251 L. Han, H. Zhou, M. Fu, J. Li, H. Ma and B. Zhang, *Chem. Eng. J.*, 2023, **473**, 145337.
252 R. T. Ginting, H. Abdullah and V. Fauzia, *Mater. Lett.*, 2022, **313**, 131779.
253 J. Su, Y. Xie, P. Zhang, R. Yang, B. Wang, H. Zhao, Y. Xu, X. Lin, J. Shi and C. Wang, *Desalination*, 2023, **566**, 116905.
254 J. Su, P. Zhang, R. Yang, B. Wang, H. Zhao, W. Wang and C. Wang, *Renewable Energy*, 2022, **195**, 407–415.
255 X. Wu, Y. Lu, X. Ren, P. Wu, D. Chu, X. Yang and H. Xu, *Adv. Mater.*, 2024, **36**, 2313090.
256 C. Chen, M. Wang, X. Chen, X. Chen, Q. Fu and H. Deng, *Chem. Eng. J.*, 2022, 137603.
257 Y. Xia, Q. Hou, H. Jubaer, Y. Li, Y. Kang, S. Yuan, H. Liu, M. W. Woo, L. Zhang, L. Gao, H. Wang and X. Zhang, *Energy Environ. Sci.*, 2019, **12**, 1840–1847.
258 H. Mo and Y. Wang, *Water Res.*, 2022, **226**, 119276.
259 Z. Song, C. Ge, Y. Song, Z. Chen, B. Shao, X. Yuan, J. Chen, D. Xu, T. Song, J. Fang, Y. Wang and B. Sun, *Small*, 2023, **19**, 2205265.
260 Y. Zhang, D. Zhao, F. Yu, C. Yang, J. Lou, Y. Liu, Y. Chen, Z. Wang, P. Tao and W. Shang, *Nanoscale*, 2017, **9**, 19384–19389.
261 A. M. Saleque, S. Ahmed, M. N. A. S. Ivan, M. I. Hossain, W. Qarony, P. K. Cheng, J. Qiao, Z. L. Guo, L. Zeng and Y. H. Tsang, *Nano Energy*, 2022, **94**, 106916.